Applied Ocean Research 97 (2020) 102078

Contents lists available at ScienceDirect

Applied Ocean Research

journal homepage: www.elsevier.com/locate/apor

Two-dimensional experimental and numerical investigations of perforated plates in oscillating flow, orbital flow and incident waves

Fredrik Mentzoni*, Trygve Kristiansen

Department of Marine Technology Norwegian University of Science and Technology NO-7491 Trondheim, Norway

ARTICLE INFO

Keywords:
Perforated plate
Added mass
Damping
Computational fluid dynamics
Experimental study

ABSTRACT

The hydrodynamic loads on two-dimensional perforated plates are investigated experimentally and numerically. Two single perforated plate configurations, consisting of rows of either circular or square cylinders, are studied. Experiments and simulations are performed for oscillating flow, orbital flow and waves. The Keulegan–Carpenter (KC) number and period of oscillation are varied. The hydrodynamic forces and coefficients are highly KC number dependent. There is in general small dependence on the period of oscillation. An exception is in wave tests where the normalized force on the structures depend on both the wave length-to-plate diameter ratios and the submergence. Added mass and damping coefficients are presented for oscillating and orbital flow conditions. The hydrodynamic force on both configurations is dominated by damping. We find in general good agreement between the experimental and numerical results.

We highlight some aspects of the influence from plate-end flow separation on the forces of the plates. A considerable reduction in the hydrodynamic forces is found in orbital motion compared to oscillating flow, increasingly so as the KC number is increased. Asymmetric flow patterns, where the vortex generation at the plate-ends occurs only on one side at a time, are observed in orbital flow, whereas the plate-end vortices from the two sides of the plate are generated simultaneously in oscillating flow. Streamline plots indicate that the relative importance of vortex generation from the plate-ends increases with increasing KC number.

1. Introduction

1.1. Structure

This is the first part of a study on the hydrodynamic loads on perforated plates in waves and oscillating and orbital flows. The focus in the first part is on the hydrodynamic forces of single perforated plates in waves compared to oscillating and orbital flows. The second part of the study is on the hydrodynamic interaction between two parallel perforated plates in oscillating and orbital flows [1]. The two parts are closely related. However, the introduction, theory and method sections are included in both parts, such that they can be read separately.

This part of the study is organized in six main sections. The first covers the present introduction with motivational background. In Sections 2–4 we present definitions of hydrodynamic coefficients, the experimental setup and the numerical methods. Results are presented and discussed in Section 5. Finally, conclusions are drawn in the last section.

1.2. Background

Safe and cost-efficient marine operations are essential for the development of subsea fields. Typically, the structures and modules of subsea fields are lifted by cranes on vessels, lowered through the water, and installed on the seabed. Operations include installation of new modules, as well as maintenance and modification of existing ones.

There is an industrial demand to perform such operations on an all-year basis. The goal is to increase the operational weather window, and thereby decrease the risk of costly delays. All-year operability implies more demanding conditions, and must be achieved together with, and not at the expense of, safe operations. Unsafe conditions can lead to drop accidents, risk for personnel and damages to the structure, crane or vessel. Consequently, there is a need for accurate estimates of the hydrodynamic forces that subsea structures are exposed to during the lifting and lowering phases in harsh environments.

Perforated plates share direct similarities with main structural elements found on complex subsea modules, e.g. hatch covers and mudmats. In particular, the perforated plate model is relevant when the structure parts are relatively wide compared to their thickness, and

* Corresponding author.
E-mail address: fredrik.mentzoni@ntnu.no (F. Mentzoni).

https://doi.org/10.1016/j.apor.2020.102078
Received 16 August 2019; Received in revised form 30 January 2020; Accepted 31 January 2020
Available online 22 February 2020

consist of many openings. The hydrodynamic forces on these structural components are likely to be dominant for the total force on the modules. In previous experimental studies within the same project, simplified subsea structures consisting of perforated plates in combination with other structural components has been studied. The total hydrodynamic force on these simplified subsea structures are typically dominated by the perforated plates; for example, we found almost no difference in the hydrodynamic coefficients of two perforated plates in parallel compared to two perforated plates in parallel with five cylinders in between [2]. Later, we developed a numerical tool for estimating the hydrodynamic forces on two-dimensional perforated structures [3], and utilized the tool to study the importance of perforation ratio and amplitude of motion on the hydrodynamic forces of perforated plates [4]. Furthermore, various mudmat configurations were investigated experimentally and numerically in a separate study [5].

In addition to protection structures found on subsea modules, perforated plates are relevant in several industrial applications; perforated structures are used as heave plates, wave absorbers, swash bulkheads and other damping plates. Consequently, there has been a great deal of work concerned with the hydrodynamics of perforated structures. A presentation was given by Molin in 2011 [6], where he summarizes relevant work on perforated structures in oscillatory flow (waves). Additionally, Molin presents the background for his semi-analytical method for calculating the hydrodynamic coefficients of perforated structures. The semi-analytical method is based on the assumption of a quadratic pressure-drop condition for the flow through the openings of the perforated structure, combined with potential flow conditions in the fluid domain. A consequence of the quadratic pressure drop condition is that the hydrodynamic coefficients of perforated structures are functions of the amplitude of motion. The method has been applied to various problems and several cases are presented and discussed, including the relevance for protection structures of subsea modules.

Among other relevant studies are the works by Sandvik et al. [7], Tao and Dray [8], An and Faltinsen [9], Li et al. [10], and Tian et al. [11]. These studies agree that experimentally obtained hydrodynamic coefficients of perforated plates depend on both the KC number and the perforation ratio, τ. In the study by Sandvik et al. [7], experimental investigations of five hatch cover models with perforation ratios $\tau = 0.15$, $\tau = 0.25$, $\tau = 0.27$, $\tau = 0.38$ and $\tau = 0.47$ were performed for $0.1 < \mathrm{KC} < 1.7$. Tao and Dray [8] performed experiments for $0.2 \leq \mathrm{KC} \leq 1.2$ of four similar circular disks with varying perforation ratios, $\tau = 0$, $\tau = 0.05$, $\tau = 0.1$ and $\tau = 0.2$. An and Faltinsen [9] investigated two similar perforated rectangular plates of $\tau = 0.08$ and $\tau = 0.16$ for $0.17 \leq \mathrm{KC} \leq 1.7$. The experimental study by Li et al. [10] included perforated rectangular plates of $\tau = 0.01$, $\tau = 0.05$ and $\tau = 0.10$ for $0.2 \leq \mathrm{KC} \leq 1.0$. The perforated disks in the study by Tian et al. [11] have perforation ratios $\tau = 0.05$, $\tau = 0.10$ and $\tau = 0.20$ and were tested for $0.15 \leq \mathrm{KC} \leq 3.15$. The following two observations are highlighted in all these studies: 1) For a given perforation ratio, increasing the KC number increase, in general, the hydrodynamic coefficients. 2) For a given KC number, increasing the perforation ratio decreases, in general, the hydrodynamic coefficients. An exception to 2) is reported by Tao and Dray [8], where the damping coefficients for small KC numbers for (relatively dense) perforated plates can be higher than corresponding solid plates. This has also been found in studies using semi-analytical [12] and numerical [4] methods.

The aim of the present study is to increase our understanding of the hydrodynamic behavior and forces on perforated structures of subsea modules in waves. In this first part of the study, single perforated plates, consisting of rows of closely spaced cylinders, with high length-to-diameter ratios, are studied. Experimental and numerical investigations of the plates in waves and oscillating conditions are performed. Additionally, orbital flow conditions in an infinite fluid domain are studied numerically. Hydrodynamic forces and coefficients are presented for a range of Keulegan–Carpenter (KC) numbers and periods of oscillation. Moreover, we include flow visualizations from our numerical simulations to highlight important physical phenomena, in particular flow separation from the plate ends.

2. Hydrodynamic forces and coefficients

Three flow conditions are considered: 1) oscillating flow, 2) orbital flow, 3) incident waves. In oscillating flow, the horizontal velocity component is zero, whereas the vertical velocity component oscillates harmonically. Note that there is a difference between the oscillating flow experiments—in which the models are forced to oscillate in otherwise calm water—and the oscillating flow numerical simulations—in which the models are fixed and the ambient velocity, set on the boundaries of the numerical domains, oscillates. In orbital flow (only numerical), both the horizontal and vertical ambient velocities oscillate harmonically. In incident waves (both experimental and numerical), the models are fixed and subjected to waves generated by a wave flap. Results are, typically, presented as functions of the Keulegan–Carpenter (KC) number. The KC numbers are based on the amplitude of the velocity in oscillating and orbital flows, and on the amplitude of the incident waves in the incident wave tests. For oscillating and orbital flows, hydrodynamic coefficients (added mass and damping) are presented. For incident wave tests, the normalized force amplitude on the models is presented. In the following, the relevant parameters are presented.

The results of the present study are presented as functions of the Keulegan–Carpenter (KC) number. For oscillating and orbital flow conditions, this is taken as

$$\mathrm{KC} = \frac{WT}{D}, \tag{1}$$

with W being the amplitude of the first harmonic of the prescribed (numerical results) or measured (experimental results) velocity, T being the oscillation period and D the characteristic dimension of the structure (width of the plate). In the present wave tests, the KC number is estimated based on the measured incident wave amplitude and the vertical distance from the mean free-surface to the structure, using linear wave theory [13],

$$\mathrm{KC} = 2\pi \frac{\zeta_a}{D} \frac{\sinh k(z_m + h)}{\sinh kh} \tag{2}$$

with ζ_a being the incident wave amplitude, z_m the z-coordinate of the center plane of the model, and h the water depth in the wave flume. $z = 0$ coincides with the still waterline. The wave number, $k = \frac{2\pi}{\lambda}$, is a function of the wave period and the water depth, according to the linear wave dispersion relation $\omega^2 = gk \tanh kh$, with $\omega = \frac{2\pi}{T}$ being the oscillation frequency. $g = 9.81\mathrm{ms}^{-2}$.

Added mass and damping coefficients are extracted from forced oscillations experiments. The models are forced to oscillate in otherwise calm water. The plates are horizontal, while the vertical force is measured. The measured hydrodynamic radiation force is decomposed into added mass and damping terms,

$$F = A\ddot{\eta} + B\dot{\eta} \tag{3}$$

with F being the measured net hydrodynamic force, A the added mass coefficient, $\ddot{\eta}$ the harmonically oscillating acceleration, B the damping coefficient and $\dot{\eta}$ the harmonically oscillating velocity. The measured force from corresponding tests without any model in the experimental rig is subtracted, time-step by time-step, in order to find the net hydrodynamic force on the models.

The added mass and damping coefficients are obtained by Fourier averaging,

$$A \int_{mT} \ddot{\eta}\ddot{\eta}\ dt + 0 = \int_{mT} F\ddot{\eta}\ dt, \tag{4}$$

$$0 + B \int_{mT} \dot{\eta}\dot{\eta}\ dt = \int_{mT} F\dot{\eta}\ dt. \tag{5}$$

Here m indicates a selected oscillation period. The forced oscillation experiments consist of 20 oscillation periods for each combination of period and amplitude. The first five periods gradually ramp the signal to its prescribed amplitude, then follows ten full cycles at the prescribed amplitude, before the signal is gradually ramped out to zero during the last five oscillations. The ramp is linear, hence the signal can be written

$$\eta = \begin{cases} \frac{t}{5T}\eta_a \sin \omega t; & 0 \le t < 5T, \\ \eta_a \sin \omega t; & 5T \le t < 15T, \\ (1 - \frac{t-15T}{5T})\eta_a \sin \omega t; & 15T \le t < 20T. \end{cases} \tag{6}$$

Here η_a is the prescribed amplitude. The mean of the oscillation cycles with the prescribed amplitude of motion, $5 < m < 15$, are used to calculate the coefficients. The variation during these 10 cycles is also investigated.

Results from the numerical simulations of oscillating and orbital flow are presented in a similar manner; coefficients and force amplitudes are based on the mean of the vertical force from the oscillation cycles with the prescribed amplitude of motion. In the numerical simulations, 30 cycles are simulated including two cycles of ramp-in of the signal. The mean of the last 25 oscillation cycles, $5 < m < 30$, are used to calculate the coefficients.

In the numerical simulations of oscillating and orbital flow, the discretized models are fixed and experience an ambient sinusoidally oscillating flow. Therefore, the total calculated force on the models consists of the hydrodynamic diffraction force and the Froude–Krylov force. In order to compare the experimental and numerical results, the Froude–Krylov force is subtracted, and the diffraction force is decomposed in a damping term, proportional to the ambient velocity, and an added mass term, proportional to the ambient acceleration, according to Eq. (3).

The results of the present study are presented in terms of dimensionless hydrodynamic coefficients and forces. The added mass and damping coefficients are made nondimensional by the corresponding analytical solid flat plate added mass,

$$A_0 = \rho \frac{\pi}{4} D^2 L, \tag{7}$$

where ρ is the density and L is the length in the lateral direction of the structure. End plates are used in the experimental investigations to yield a near two-dimensional setup. Therefore, A_0 is taken as the two-dimensional analytical added mass times L. The numerical simulations are two-dimensional and Eq. (7) is used without the multiplication of L.

From Eqs. (3) and (7), an expression for the normalized hydrodynamic force can be obtained for the case of a harmonically oscillating plate velocity $w = W \sin \omega t$,

$$\frac{F}{\omega W A_0} = \sqrt{\left(\frac{A}{A_0}\right)^2 + \left(\frac{B}{\omega A_0}\right)^2} \sin(\omega t + \phi). \tag{8}$$

Here ϕ is the phase difference between the velocity and the normalized force. If the plate is fixed and the water is oscillating, a corresponding expression for the normalized force amplitude including the Froude–Krylov contribution is

$$\frac{F_a}{\omega W A_0} = \sqrt{\left(\frac{A + \rho V}{A_0}\right)^2 + \left(\frac{B}{\omega A_0}\right)^2}. \tag{9}$$

A similar expression can be obtained for the vertical force on a structure fixed in waves,

$$\frac{F_a}{\omega W A_0} = \frac{F_a}{\omega^2 \zeta_a A_0} \frac{\sinh kh}{\sinh k(z_m + h)}. \tag{10}$$

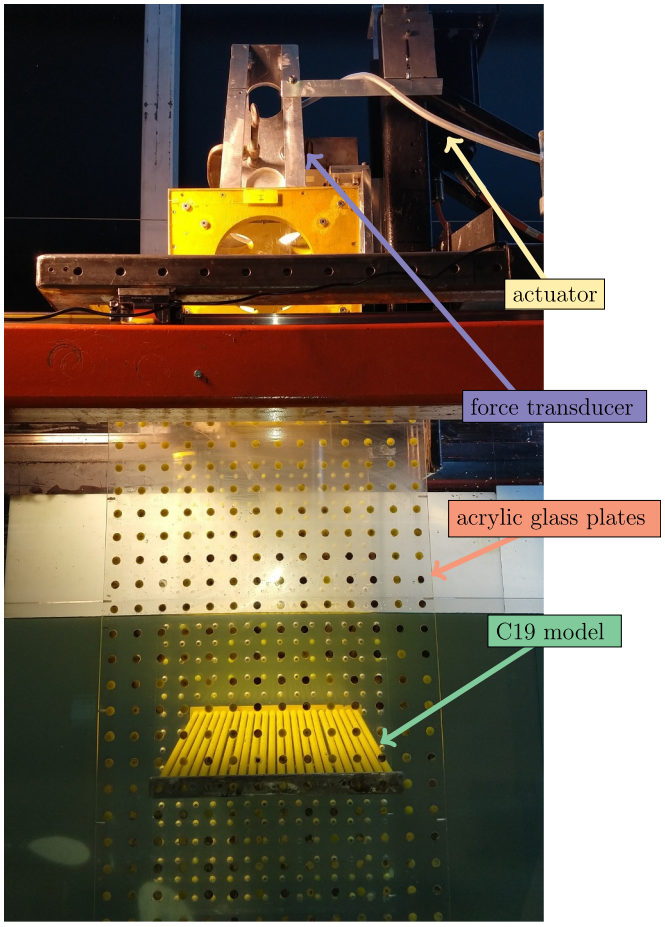

Fig. 1. Photo of the present experimental test setup. Perforated structure consisting of circular cylindrical pipes (C19) placed inside the acrylic glass plates of the experimental rig.

3. Experiments

Experimental investigations of two different types of structures, consisting of rows of cylinders, are performed in a wave flume at the Marine technology center in Trondheim, Norway. The tank is approximately 13.5 m long and 0.60 m wide. A rig is placed in the middle of the tank. The rig consists of two acrylic glass plates, parallel to the tank walls, fastened to a wooden box on the top end, that is connected to a steel frame. The steel frame is connected to a 6 kN force transducer connected to an actuator on the top. The acrylic glass plates act as endplates, which yields a near two-dimensional setup. The gap between the acrylic glass plates and the tank walls are 9 mm. The tested models are installed through screw holes in the acrylic glass plates. Yellow putty is used to fill holes that are not used. The setup allows for testing a large range of structures in different orientations and placements, and has previously been used in experimental investigations of ideal perforated plates, cylinders, simplified mudmats and subsea structures [2,3,5]. A photo of the rig, with a perforated structure consisting of circular cylindrical pipes fastened inside the acrylic glass plates, is presented in Fig. 1.

The software package Catman Easy by HBM is used for data acquisition of the experimental measurements. Measurements of the vertical force, motions and wave elevations are sampled at 200 Hz with Butterworth filtering at 20 Hz. The measurements are band-pass filtered around the basic harmonic of the oscillation when calculating the wave elevations, hydrodynamic coefficients and normalized hydrodynamic force amplitude. The applied instrumental setup was carefully set up to achieve zero phase delay between the different signals, in order to

obtain reliable hydrodynamic force coefficients.

Two types of experiments are conducted: 1) Forced oscillation tests where the models are forced to oscillate in otherwise calm water. 2) Regular wave tests where the models are fixed and experience forces due to incident waves. Descriptions of the tested models and experimental conditions are given in the following sections.

3.1. Configurations

Two perforated plates are experimentally investigated. We use the abbreviations C19 (circular cylinders, perforation ratio $\tau = 0.19$) and S28 (square cylinders, perforation ratio $\tau = 0.28$) when referring to the two structures throughout the text. C19 is $D =$ 298 mm wide and consists of 24 equal circular cylinders of 10 mm diameters. The circular cylinders are made from aluminum and have wall-thicknesses of 2 mm. S28 is $D =$ 360 mm wide and consists of 26 equal cylinders with square cross-section of 10 mm $\times$ 10 mm. The square cylinders are made from aluminum and have wall-thicknesses of 1 mm. 24 (C19) and 26 (S28) cylinders are used, hence, the two perforated plates consist of 23 (C19) and 25 (S28) openings. The perforation ratios are calculated as

$$\tau = \frac{\text{Open area}}{\text{Total area}} = 1 - \frac{nd}{D}, \tag{11}$$

with n being the number of cylinders, d being the diameter of each cylinder and D being the width of the structure. The width-to-thickness ratios are $\frac{D}{t} = 30$ (C19) and $\frac{D}{t} = 36$ (S28). All structure parts are $L = 0.57$ m long, such that they fit inside the acrylic glass plates of the experimental rig. Photos of C19 and S28 are presented in Fig. 2. Schematic descriptions are presented in Fig. 3; details are given in Table 1.

3.2. Forced oscillation tests

In the first part of the experimental investigations, the perforated plates are forced to oscillate harmonically in otherwise calm water. Forced heave motion (vertical oscillations) is considered. A sketch of the setup is presented in Fig. 4. The models are placed in the middle of the tank in the forced oscillation tests; the center of the model is 0.5 m from the free surface and the bottom of the tank, and approximately 6.5 m from the end walls of the wave flume. The water depth is $h = 1.0$ m. Parabolic beaches, to damp out radiated waves, are placed on both ends of the tank. The top of the beaches are set 2 mm below the free surface.

We measure the vertical motions, vertical force and wave elevations during the forced oscillation tests. The test series include five oscillation periods, $T =$ 1.00 s, 1.25 s, 1.50 s, 1.75 s and 2.00 s, and a range of amplitudes from 1.7 cm to 13 cm, corresponding to $0.3 \lesssim \text{KC} \lesssim 3$, depending on the structure. The experimental results are presented with different markers for the five forcing periods, diamonds ($T =$ 1.00 s), pentagons (1.25 s), hexagons (1.50 s), circles (1.75 s) and stars (2.00 s). Several accelerometers are used to monitor both the (wanted) vertical and (possible) horizontal motions of the configurations.

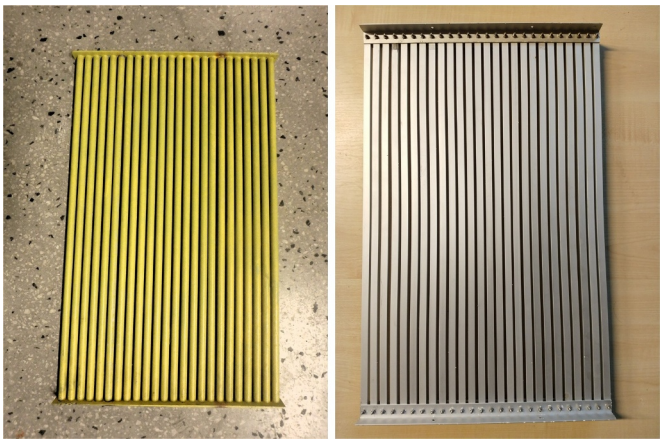

Fig. 2. Photos of C19 (left) and S28 (right) used in present experimental investigations. The plates are 0.57 m long. The width of the plates are $D = 0.298$ m (C19) and $D = 0.360$ m (S28).

The present experimental setup yields conditions that are close to an infinite fluid domain. Nevertheless, since the water depth is limited to $h = 1.0$ m, some influence from the boundaries should be expected. The increase in added mass coefficient for a circular cylinder close to the free-surface or a wall is discussed by Faltinsen [13, p. 54]. When the distance to the boundary is larger than the diameter of the cylinder, the increase in the added mass of the cylinder is rather small, around 10% and decreasing for increasing distance [13, Fig. 3.11]. In the present experimental investigations, the distance to the boundaries (50 cm) is larger than the width of the largest plate (36 cm). Further, the added mass of perforated plates is small at small KC numbers since the openings allow water to flow without circumventing the plate. However, for larger KC numbers, the added mass increases rapidly due to blocking of flow through the perforated openings. Moreover, the oscillating plate will generate waves that have some influence on the hydrodynamic coefficients. The radiated waves are measured by wave probes downstream of the rig. The corresponding wave-radiation damping coefficients [13, p. 47], are small for all tested forcing amplitudes and periods of oscillation for both C19 and S28. We conclude from this that the setup yields conditions that are close to an infinite fluid domain.

3.3. Regular wave tests

A wave flap at the left end of the wave flume is used to generate regular waves in the second part of the experiments. A sketch of the regular wave setup is presented in Fig. 5. The water depth is $h = 1.0$ m in all tests. The wave flap is hinged 0.1 m above the bottom of the tank. The flap is forced to oscillate harmonically with a prescribed amplitude and period of oscillation. Four wave periods are applied, $T = 1.0$ s, 1.1 s, 1.2 s and 1.3 s. The flap amplitudes are varied to yield waves with wave amplitudes from 2.1 cm to 6.5 cm, corresponding to wave steepnesses in the range $\frac{1}{38} \lesssim \frac{H}{\lambda} \lesssim \frac{1}{20}$. The regular wave tests are performed with the models placed at three vertical positions, $z_m = -0.30$ m, $z_m = -0.20$ m and $z_m = -0.10$ m. Hence, the models are placed closer to the mean free-surface in the regular wave tests than in the forced oscillation tests.

The wave elevations are measured by eight wave probes placed in pairs at four locations in the tank: 3.5 m, 2.0 m and 0.4 m upstream of the rig, and 2.0 m downstream of the rig, cf. Fig. 5. In our analysis, we use the incident (undisturbed) vertical water particle velocity velocity at the geometrical center of the model as nondimensional parameter. The wave profile above the model center is estimated based on the upstream wave probes. Wave probes 1–6 are used to estimate the wave celerity, and the measurements of wave probes 1–4 are used to estimate the wave profile above the geometrical center of the models. Special care is taken to ensure correct measurements of the horizontal distances between the upstream wave probes and the position of the geometrical center of the models, essential for calculating the correct wave celerity and phase of the wave at the position of the models.

In both the experimental and numerical wave investigations, two cycles of oscillation are used to ramp the wave flap to its prescribed amplitude of motion. We ignore the following three cycles of oscillation, i.e. in total five cycles including the ramp, in order to achieve steady-state conditions. The presented results from the wave tests are based on the mean result from the following wave periods. The applied number of considered wave periods are eleven ($T = 1.0$ s), nine (1.1 s), seven (1.2 s) and five (1.3 s). Bars in the figures represent the standard deviation between the results obtained from the different wave periods.

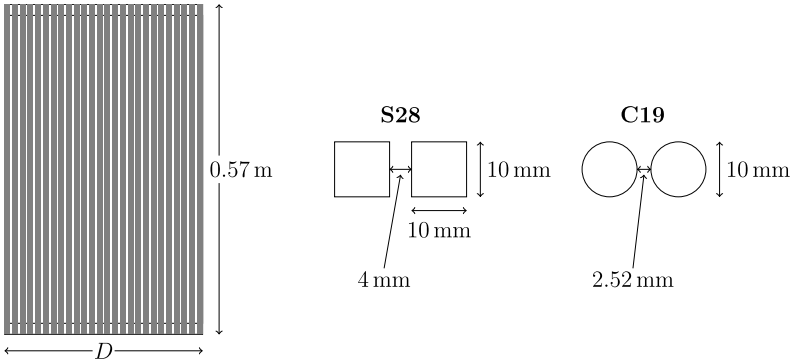

Fig. 3. Schematic sketches of S28 and C19. $D = 0.298$ m and the number of cylinders is 24 for C19, whereas $D = 0.360$ m and the number of cylinders is 26 for S28.

Table 1
Characteristics of the presently experimentally tested perforated structures. d expresses the diameter of each cylinder of C19/S28. D is the total width of the structure. M is the dry weight of the structure.

	Perforation	Cylinders	d	Openings	D	M
C19	$\tau = 1 - \frac{240\text{ mm}}{298\text{ mm}} = 0.19$	Circular	10 mm	23	298 mm	3.02 kg
S28	$\tau = 1 - \frac{260\text{ mm}}{360\text{ mm}} = 0.28$	Square	10 mm	25	360 mm	1.79kg

3.4. Reynolds numbers

The forces on blunt bodies without sharp edges, such as the circular cylinders of the C19 plate, must be expected to be Reynolds number dependent due to the lack of fixed flow-separation points. The relevant Reynolds and KC numbers are local, that is, they are based on the width of each cylinder, d. The local Reynolds number is

$$\mathrm{Re}_d = \frac{Wd}{\nu}. \tag{12}$$

The local KC number, KC_d, is

$$\mathrm{KC}_d = \frac{WT}{d}. \tag{13}$$

The range of amplitudes and periods of oscillation in the forced oscillation tests corresponds to $7.4 < \mathrm{KC}_d < 85$ and $5.3 \times < 10^2 < \mathrm{Re}_d < 4.9 \times 10^3$. The effective local Reynolds and KC numbers will be larger due to the flow restriction, caused by the row of cylinders, which will increase the speed of the flow around each cylinder. Using a simple control volume analysis, the increase can be estimated to $\frac{1}{\tau} \approx 5$, that is, $37 \lesssim \mathrm{KC}_d \lesssim 425$ and $2.7 \times 10^3 < \mathrm{Re}_d < 2.5 \times 10^4$. These estimated KC_d and Re_d numbers are likely conservative since the flow will circumvent the plate. Nevertheless, even if the range of Reynolds numbers are extended to include somewhat smaller values than 2.7×10^3, the drag coefficient for a smooth circular cylinders varies only slightly in this Reynolds number range. One may expect similar behavior for the present model. For moderate to large KC numbers, we expect the global wake, i.e. that shed from the two cylinders at the ends of the model, to dominate the hydrodynamic force on the plate, and the effect of the placement of the separation point on each cylinder to be negligible.

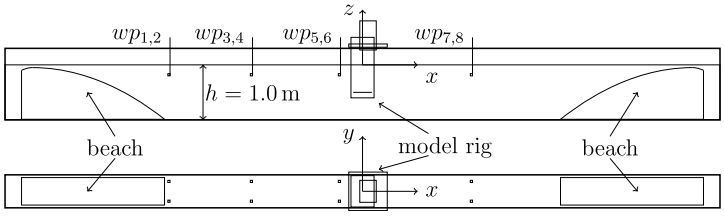

4. Numerical simulations

Numerical results (CFD) are obtained from a two-dimensional Navier–Stokes solver, developed earlier in our study [3]. The numerical simulations are performed for discretized models of S28. The CFD uses a staggered grid approach. The governing equations are solved on rectilinear grids with a fine resolution region close to the discretized perforated plates, and gradually larger cells away from the structure. We follow previous findings using the CFD for simulation of perforated plates, regarding grid size and stretching, the size of the numerical domains and the number of fluid cells between each plate element [3,4]. In particular, the numerically obtained force coefficients of perforated plates are almost insensitive to changes of the fine region grid cell size between cell sizes of 4 mm, 2 mm and 1 mm [3]. Further, using two fluid cells in the openings between two adjacent plate elements is sufficient and give similar results as using more fluid cells in the openings [3,4]. We have also found that the hydrodynamic coefficients are almost insensitive to the number of holes on the plate; modeling a perforated plate of $\tau = 0.19$ using six holes instead of 13 or 26 gives only small differences in the coefficients [3]. An exception is for very small KC numbers, in which the hole size relative to the plate size is the important parameter for the added mass of a perforated plate; increasing the number of holes (n_h) will reduce the added mass as $\frac{1}{n_h}$ for $\mathrm{KC} \to 0$ [4,6].

The present CFD solves the governing equations of isothermal flows of a homogeneous Newtonian fluid with negligible bulk viscosity, the continuity and momentum equations, by use of a fractional-step method, as that by Chorin [14], where the momentum equation is split into two steps,

$$\frac{u_i^* - u_i^n}{\Delta t} = -u_j \frac{\partial u_i}{\partial x_j} + \nu \frac{\partial^2 u_i}{\partial x_j^2}, \tag{14}$$

$$\frac{u_i^{n+1} - u_i^*}{\Delta t} = -\frac{1}{\rho}\frac{\partial p}{\partial x_i}. \tag{15}$$

Standard index notation is used; u_i represents the velocity component in the x_i direction. For simplicity, the velocity components are referred to as $u = u_1$ (horizontal direction) and $w = u_2$ (vertical direction). The fluid density, ρ, and kinematic viscosity, ν, are set to values similar to the water properties of the experimental investigations, $\rho = 1000\ \mathrm{kgm^{-3}}$ and $\nu = 1 \times 10^{-6}\mathrm{m^2 s^{-1}}$. n represents the present time-step,

Fig. 4. Sketch of the tank setup during forced oscillation tests. Upper: Side view. Lower: Bird's eye view. The tank is approximately 13.5 m long and 0.60 m wide. The water depth is $h = 1.0$ m. The position of the model rig, wave probes and beaches are indicated.

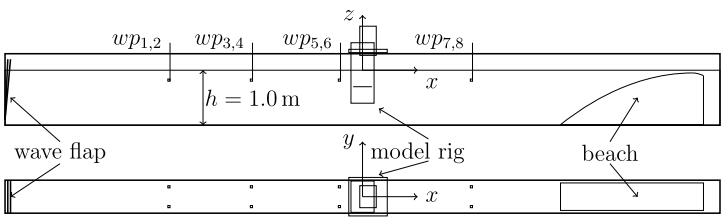

Fig. 5. Sketch of the tank setup during incident wave tests. Upper: Side view. Lower: Bird's eye view. The tank is approximately 13.5 m long and 0.60 m wide. The water depth is $h = 1.0$ m. The position of the wave flap, model rig, wave probes and beach are indicated.

$n + 1$ the next time-step, and * an auxiliary step. Since the velocity field at $n + 1$ is divergence free, the divergence of Eq. (15) yields a Poisson equation for the pressure, p,

$$\frac{\partial^2 p}{\partial x_i^2} = \frac{\rho}{\Delta t}\frac{\partial u_i^*}{\partial x_i}. \tag{16}$$

In simulations of oscillating and orbital flow, for each time-step, Eq. (14) is solved to find the tentative velocity field. Then Eq. (16) is used to determine the pressure, before the velocity field at $n + 1$ is found from Eq. (15). The three steps of the procedure are as follows:

1. u^n, $w^n \rightarrow u^*$, w^*
2. u^*, $w^* \rightarrow p^{n+1}$
3. u^*, w^*, $p^{n+1} \rightarrow u^{n+1}$, w^{n+1}.

Spatial discretizations in the CFD are of first and second orders. The diffusion terms of Eq. (14), the pressure gradient terms of Eq. (15), as well as the terms of Eq. (16), are solved with second-order accurate central difference schemes unless else is explicitly highlighted. The spatial discretization of the advection terms is performed using the first order upwind scheme. The advection terms are linearized in time using the previous known velocity, i.e. u_j^n of Eq. (14).

Time-stepping is performed using the implicit Euler scheme. The time-step size is chosen based on requirements to ensure at least 200 time-steps per period of oscillation, and a CFL number smaller than one in all cells,

$$\Delta t = \min\left(\frac{T}{200}, \frac{\Delta x}{u}, \frac{\Delta z}{w}\right). \tag{17}$$

Simulations are performed with two different discretizations of S28. Illustration of the fine regions of the two grids are presented in Figs. 6 and 7. The first discretization is an exact two-dimensional numerical model with the same geometrical cross-section as the structure that is experimentally investigated, i.e. 26 cylinders, cf. Fig. 2. Additionally, simulations are performed with a simplified numerical model, denoted S28s. S28s has a coarser grid and less structure elements, 11 vs. the 26 cylinders of the physical model, but the same perforation ratio. A major advantage of the coarser grid model is increased numerical stability in simulations with incident waves. For consistency, simulations with S28s in oscillating and orbital flow conditions are also conducted.

4.1. Oscillating flow conditions

The boundary conditions in oscillating flow are illustrated in Fig. 8. In oscillating flow conditions, the velocity field at the borders of the computational domain is set to a prescribed oscillating vertical velocity based on a prescribed velocity amplitude, W, which from Eq. (1) can be written in terms of the KC number, the period of oscillation, T, and the characteristic width of the structure, D,

$$u = 0, \tag{18}$$

$$w = \frac{D}{T}\mathrm{KC}\sin\omega t. \tag{19}$$

The period of oscillation (and corresponding circular frequency $\omega = \frac{2\pi}{T}$) is set to $T = 1.0$ s to yield similar Reynolds numbers as in the experiments, although the Reynolds number is expected not to be of importance since the cylinders have sharp edges. Hence $\frac{D}{T}$ is a constant, 0.36 ms^{-1}, in all oscillating flow simulations.

Appropriate boundary conditions for the pressure gradient are obtained from the Navier–Stokes equation,

$$\frac{\partial p}{\partial x} = -\rho\frac{\partial u}{\partial t} = 0, \tag{20}$$

$$\frac{\partial p}{\partial z} = -\rho\frac{\partial w}{\partial t} = -\rho\omega\frac{D}{T}\mathrm{KC}\cos\omega t. \tag{21}$$

No-slip conditions are used on the boundaries of the discretized models,

$$u = w = 0, \quad \frac{\partial p}{\partial x} = \frac{\partial p}{\partial z} = 0. \tag{22}$$

4.2. Orbital flow conditions

The boundary conditions in orbital flow are illustrated in Fig. 9. Except for non-zero horizontal prescribed velocities and accelerations, the orbital flow simulations are performed in the exact same manner as the oscillating flow simulations. The following velocity conditions are

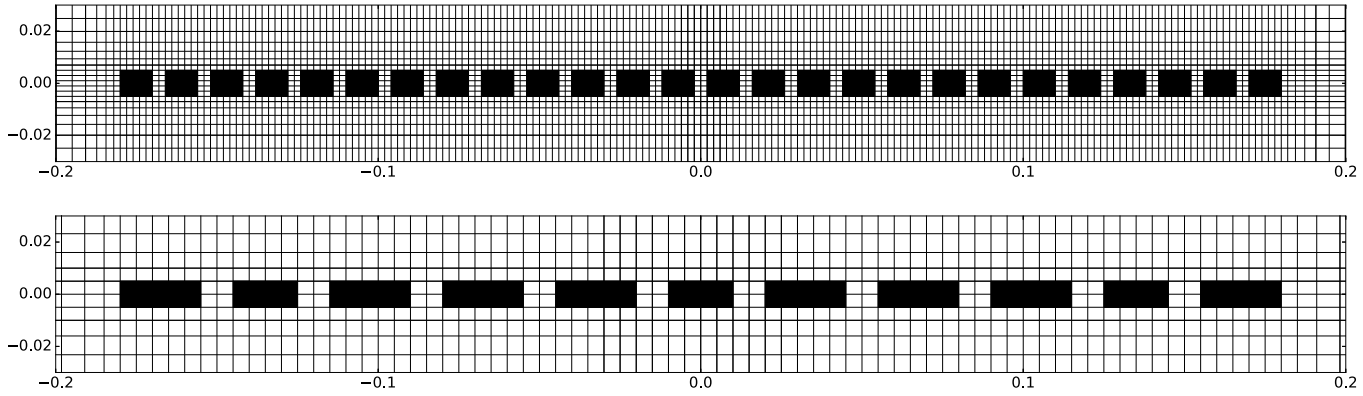

Fig. 6. Fine region grids of S28 (top) and S28s (bottom). In oscillating and orbital flow simulations, the total domain size is 6m × 6m and the total number of grid cells are 48 630 (S28) and 28 456 (S28s).

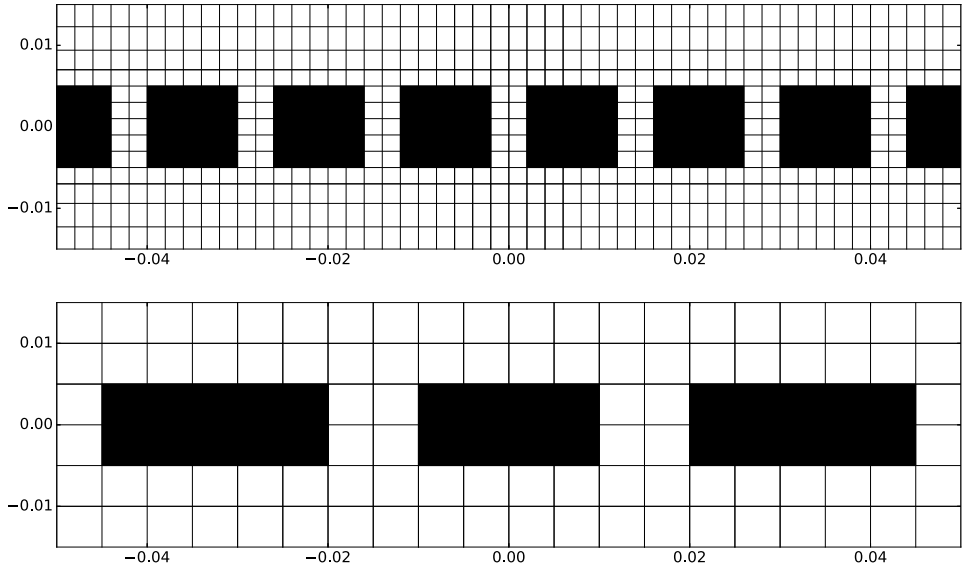

Fig. 7. A zoomed-in section of the fine region grids of S28 (top) and S28s (bottom), cf. Fig. 6.

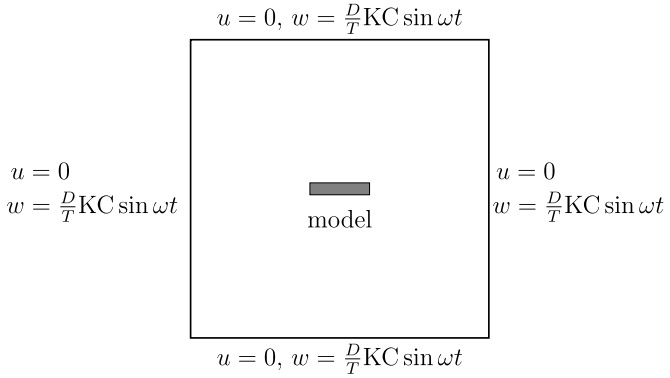

Fig. 8. Oscillating flow setup. The ambient vertical velocity component is oscillating harmonically on the boundaries. The simulated model is placed in the center of the numerical domain.

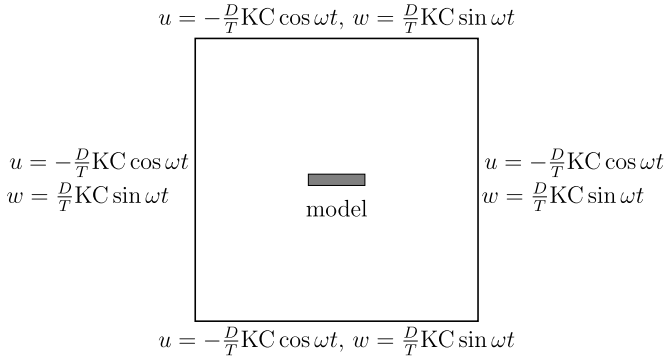

Fig. 9. Orbital flow setup. The ambient horizontal and vertical velocity components are oscillating harmonically on the boundaries. The simulated model is placed in the center of the numerical domain.

set on the boundaries of the computational domains,

$$u = -\frac{D}{T}\mathrm{KC}\cos\omega t, \tag{23}$$

$$w = \frac{D}{T}\mathrm{KC}\sin\omega t, \tag{24}$$

with corresponding appropriate boundary conditions for the pressure gradient based on the prescribed accelerations.

Orbital flow conditions may be regarded as a limiting case of a body submerged in waves, where the wave is long compared to the model and the model is deeply submerged, such that there is no interaction with a free surface. A benefit of this approach is that simulations with model in waves can be set up similar to oscillating flow conditions. Later in the text, we compare results in orbital flow with both oscillating flow results and results from wave tests and simulations using a free surface.

4.3. Simulations with incident waves

The final set of numerical simulations are performed using a numerical wave tank based on a hybrid Navier–Stokes and potential-flow approach, similar to [15]. In a few layers of cells close to the top surface, i.e., the free surface, the advection and diffusion terms of Eq. (14) are omitted. Consequently, the right-hand side of Eq. (16) is zero. Kristiansen and Faltinsen [15] noted that no vorticity of significance should be advected into the part of the domain without consideration of the advection and diffusion terms. Sensitivity analyses of the intersection between the two parts of the domain are performed. Independent results are obtained between intersections $z = -0.075$ m, $z = -0.05$ m and $z = -0.025$ m. In the present simulations, we set the intersection between the two parts of the domain at $z = -0.05$ m such that there are 10 cell layers without advection and diffusion (the vertical grid cell size is $\Delta z = 5$ mm in this region). In addition to Eqs. (14)–(16), a differential equation for the wave elevation, ζ, solved at the free-surface boundary, is obtained from linearizing the kinematic free-surface condition. A forward Euler step is used to time-step the wave elevation,

$$\frac{\zeta_i^{n+1} - \zeta_i^n}{\Delta t} = w_i^n - b\zeta_i^n. \tag{25}$$

A numerical beach is implemented through the function $b(x)$ which is a third-order polynomial with non-zero values in the right part of the domain (opposite side to the wave flap), and zero elsewhere.

The pressure at the top boundary is obtained from the linearized Bernoulli equation,

$$p = \rho g \zeta. \tag{26}$$

Here g=9.81m s^{-2}. An appropriate boundary condition for the pressure gradient at the top boundary is taken from a first-order spatial backwards differential,

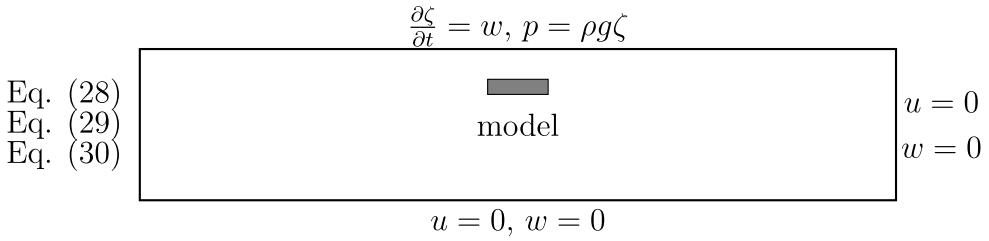

Fig. 10. Incident wave setup.

$$\frac{\partial p}{\partial z} = \frac{\rho g \zeta - p_c}{0.5 \Delta z_c}, \tag{27}$$

with p_c being the pressure in the cell center of the grid cell next to the top boundary, and Δz_c being the vertical grid cell size.

When simulating waves, the solution procedure consists of four main steps:

1. u^n, $w^n \rightarrow u^*$, w^*
2. ζ^n, $w^n \rightarrow \zeta^{n+1}$
3. u^n, w^n, u^*, w^*, $\zeta^{n+1} \rightarrow p^{n+1}$
4. u^n, w^n, u^*, w^*, ζ^{n+1}, $p^{n+1} \rightarrow u^{n+1}$, w^{n+1}.

Steps 1 and 2 are independent on each other and can be solved in the opposite sequence.

The numerical domains, used when simulating waves, are similar in size as the experimental counterparts, cf. Fig. 5. A sketch of the numerical setup is presented in Fig. 10. The right and bottom wall of the tank is modeled as solid walls with no-slip boundary conditions. A harmonically oscillating horizontal velocity is prescribed at the left boundary of the computational domain, to mimic the wave flap of the experiments. The wave flap is modeled using a prescribed harmonically oscillating horizontal velocity with amplitude U,

$$u = \begin{cases} U \sin \omega t \dfrac{z + h_f}{h_f}, & z \geq z_{FS} - h_f \\ 0, & z < z_{FS} - h_f. \end{cases} \tag{28}$$

$$w = 0 \tag{29}$$

$$\frac{\partial p}{\partial x} = -\rho \frac{\partial u}{\partial t} = \begin{cases} -\rho \omega U \cos \omega t \dfrac{z + h_f}{h_f}, & z \geq z_{FS} - h_f \\ 0, & z < z_{FS} - h_f. \end{cases} \tag{30}$$

The wave flap is hinged 0.9 m below the free surface in the experimental investigations, and the same flap design is used in the numerical simulations, i.e. $h_f = 0.9$ m ($z_{FS} = 0$).

Simulations using wave flap conditions are performed for S28s, the coarser model of the S28 plate. Stability issues were experienced in trials of the original model with finer grid, S28. We tested decreasing the time-step size and increasing the order of the time-stepping, using a fourth order Runge–Kutta scheme, but still experienced unstable simulations. We do not experience these stability issues in simulations with oscillating and orbital flow conditions. Therefore, we suspect that the problems are related to the hybrid coupling and free-surface modeling. The fine region grid size must be 2mm in order to have two grid cells between each cylinder of S28. In the coarser model, the smallest grid size is 5mm. Using larger grid cell sizes increases the general stability in terms of smaller CFL and increased numerical damping. Additionally, since a stretched grid is applied, the differences between grid sizes in the x- and z-directions are generally smaller, and less stretching is required.

4.4. Potential flow added mass calculation

Added mass coefficients in the limit of zero KC are computed with a previously developed source method, i.e. a boundary element method (BEM). The BEM is two-dimensional and based on constant source strengths. Calculations are performed for the three considered configurations—C19, S28 and S28s.

The potential flow solver is verified and checked for convergence for a single circular cross-section and a single square cross-section. The results of the convergence study of the potential flow solver are presented in Table 2. We find convergent results for both a circular and a square cross-section when increasing the number of sources to calculate the added mass of the basic structures. When we use 128 sources to discretize the basic structures, the error is less than or equal to 1% when compared with the analytical added mass of both basic structures [16, pp.145–146]. Consequently, we use 128 sources for each cylinder when modeling the perforated structures consisting of rows of circular (C19) or square (S28) cylinders, in the present study. The total number of sources in the potential flow calculations are 3072 (C19), 3328 (S28) and 1408 (S28s).

5. Results

5.1. Oscillating and orbital flows

5.1.1. Pressure distribution on a perforated plate

The pressure distribution on the perforated plate S28 is investigated using BEM and CFD and compared with BEM of a corresponding solid plate. The presently investigated perforated plates consist of small cylinders placed next to each other. Numerically, we model a perforated plate as a series of small two-dimensional plate elements with openings between them. In Fig. 11, we compare the pressure distribution on the plate elements in BEM and CFD. For a given $\frac{x}{D}$ along the plate, we present the pressure loss, that is, the upstream pressure minus the downstream pressure. In the CFD, the pressure on the plate is obtained at the time-instant $\frac{t}{T} = 30.00$, that is, when the prescribed ambient acceleration is at its maximum, and the prescribed ambient velocity is zero. We normalize using the maximum and minimum pressure losses along the plate. By utilizing the present normalization, using the

Table 2
Convergence study of potential flow solver. Added mass coefficients for a single circular cross-section and a single square cross-section calculated using an increasing number of sources to discretize the bodies. Analytical results: 1 and 1.513 for, respectively, a circular and a square cross-section [16, pp. 145–146].

Number of sources	Circular	Square
8	1.0908	1.6799
16	1.0671	1.5748
32	1.0386	1.5362
64	1.0205	1.5219
128	1.0105	1.5165
256	1.0053	1.5144
512	1.0027	1.5137
1024	1.0013	1.5134
2048	1.0007	1.5132

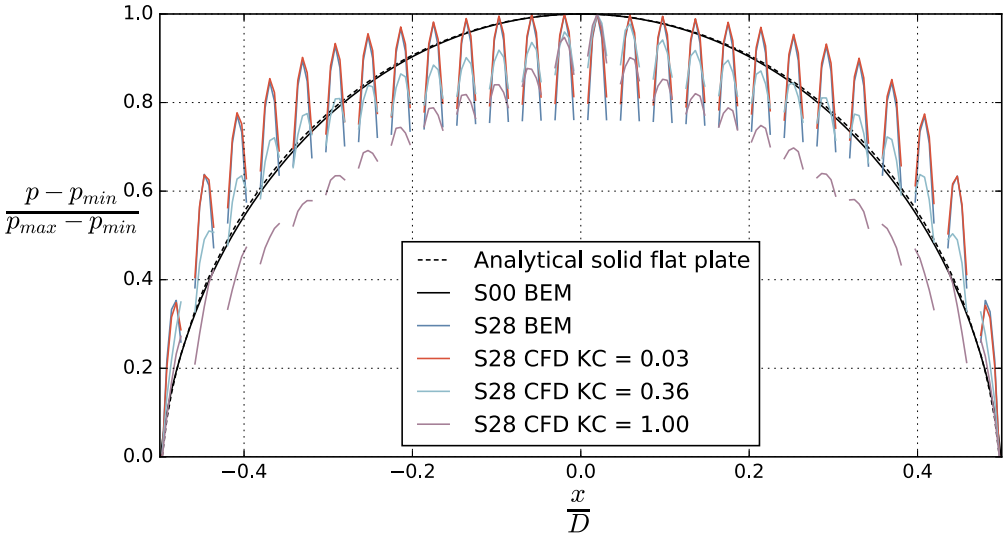

Fig. 11. Pressure loss distribution on the S28 perforated plate with BEM and CFD. The pressure loss, that is, the upstream pressure minus the downstream pressure, is normalized using the maximum and minimum pressure losses on the plate. The BEM result for a corresponding solid plate, S00, and the analytical expression for a solid flat plate, Eq. (31), are included for comparison.

maximum and minimum pressure from each calculation, we are able to visualize and compare the difference between a solid plate and a perforated plate.

The distribution of sources in the BEM matches the number of cells in the CFD. In the CFD, the sides of each plate element of S28 have five grid cells, cf. Fig. 7. Therefore, we present the calculated pressure loss based on the five grid cells above and below each plate element. In the BEM, we model each plate element using five sources along each side of the element, and present the pressure loss for the five sources above and below each plate.

Potential flow results are presented for both the S28 model and a corresponding solid plate. The analytical velocity potential for a flat plate yields a reversed U-shaped pressure distribution over the plate [13, pp. 285–286],

$$p = \rho \frac{\partial w}{\partial t} \sqrt{\frac{D^2}{4} - x^2}, \quad -\frac{D}{2} < x < \frac{D}{2}. \tag{31}$$

The global pressure loss distribution predicted by the BEM for S28 has the same characteristic reversed U-shape. Further, the pressure loss distribution over each plate element also follows the same shape. This may perhaps be anticipated.

Included in Fig. 11 are CFD results from the forced oscillation simulations at three KC numbers. For the smallest KC number, the difference between the pressure predicted by the CFD and BEM is hardly visible. This serves as further verification of the CFD. The variations in pressure loss on each plate element are, in general, smaller when the KC number is increased, that is, the significance of the local reversed U-shapes are decreased. Hence, the wake behind each plate element results in a more uniform pressure distribution, similar to the near uniform base drag pressure profile in the wake of a cylinder. For the very last plate elements, that is, the plate-ends, instead of a local reversed U-shape, the normalized pressure loss distribution is similar to that of the solid plate at the corresponding locations.

5.1.2. Added mass calculations with BEM

The potential flow added mass for C19 and S28 are presented in Table 3. C19 and S28 are exact discretizations of the experimentally investigated plates, cf. Fig. 2. S28s is a simpler and coarser version of the S28 model, cf. Fig. 6.

5.1.3. Experimental and numerical added mass and damping

The different markers of the forced oscillation experiments indicate the five tested forcing periods, $T = 1.00$ s (diamonds), 1.25 s (pentagons), 1.50 s (hexagons), 1.75 s (circles) and 2.00 s (stars). We use the same markers to indicate the periods of oscillations from the forced

Table 3
Potential flow solver added mass results (BEM) and Froude–Krylov contributions. S28 is an exact two-dimensional discretization of the S28 model, while S28s is a simplified coarser model, cf. Fig. 6. V is the volume of the structure.

	C19	S28	S28s
$\frac{A}{A_0}$	0.0780	0.0799	0.1086
$\frac{\rho V}{A_0}$	0.0270	0.0255	0.0255
$\frac{A+\rho V}{A_0}$	0.1050	0.1054	0.1341

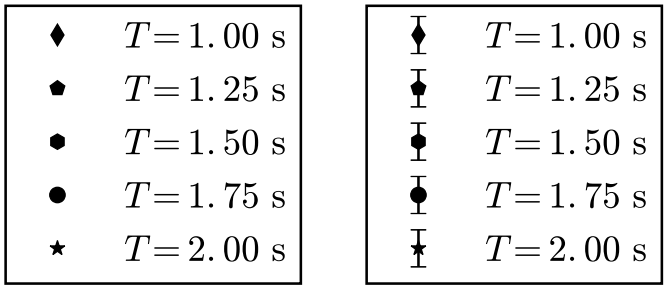

Fig. 12. Markers used to present results of different periods of oscillation from forced oscillation experiments.

oscillation experiments in all figures. The markers are presented with and without error bars in Fig. 12.

Added mass and damping coefficients from the forced oscillation tests are presented in Fig. 13. Examples of time-series from the forced oscillation tests are given in Appendix A. The coefficients increase with increasing KC for both C19 and S28. There is in general small period dependence. The coefficients for C19 are larger than those for S28. Note that the damping coefficients are larger than the added mass coefficients.

For S28, the experiments and CFD are in general in good agreement. This provides validation of the CFD, and, in addition, confidence in our experimental data. The added mass coefficients agree well for all tested KC numbers, while the damping coefficients are slightly over-predicted by the CFD. In the CFD, the structure elements have sharp-edged corners exactly equal 90°. The physical model consists of square sectional tubes (type: Alberts 4004338473518). Blunting of the edges leads to slightly less sharp corners in the physical model, a possible reason for the small discrepancy. Extrapolation of the experimental and CFD results for $KC \to 0$ is consistent with the BEM, providing further

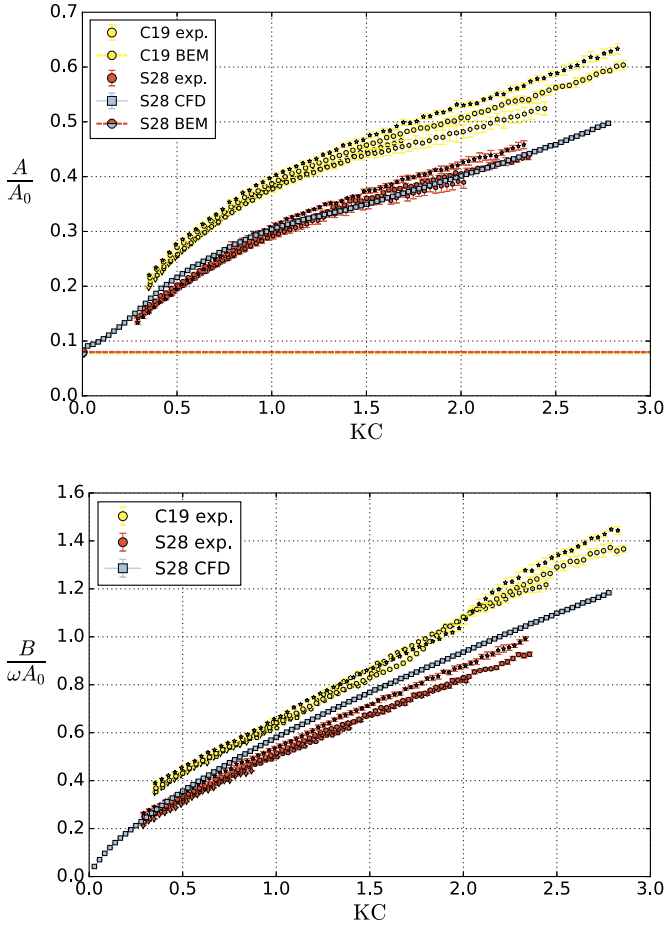

Fig. 13. Added mass and damping coefficients from forced oscillation experiments of C19 and S28 (five different periods of oscillation). Numerical results in terms of potential flow (BEM) added mass results for C19 and S28, and CFD results for S28.

confidence in the experimental setup and CFD.

5.1.4. Cylinder shape importance

The difference between C19 and S28 is both the perforation ratio and the shape of the cylinders. Consequently, it is hard to know which factor is more important for the change in hydrodynamic

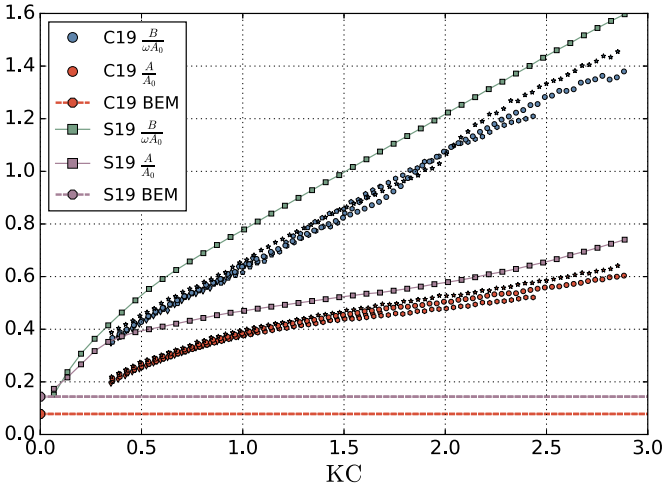

Fig. 15. Added mass and damping of the numerical simulations of S19 compared with the experimental investigations of C19.

coefficients—change of perforation ratio or change of cylinder shape.

To investigate the effect of cylinder shape, viscous flow solver simulations, and potential flow added mass calculation, are performed for a numerical model that is similar to C19, but with square, not circular, cylinders. This model is denoted S19. The numerical simulations are set up similar to those of S28. The potential flow added mass of S19 is calculated with the BEM using 128 sources per cylinder, in total 3072, equivalent to the number of sources used for C19. In the viscous flow solver simulations, the total domain size is 6m × 6 m, the fine region grid cell size is 1.25 mm, the plate width is 297.5 mm and the total number of grid cells in the domain is 59 904. The fine region grid of S19 is presented in Fig. 14.

Note the minor difference in the distance between adjacent cylinders in S19 (2.5 mm) compared to C19 (2.52 mm, to two decimal places), cf. Fig. 3. In order to use a constant grid cell size in the fine region of S19, the distance between each cylinder is set to 2.5 mm in the numerical simulation. Consequently, there is a slight difference in the width of the plates and the perforation ratio, $D = 298$ mm, $\tau = 0.1946$ (C19) versus $D = 297.5$ mm, $\tau = 0.1933$ (S19). However, these differences are very small and within the expected error of measuring the correct width of C19; needless to say, these differences are without importance for the present comparison.

Comparing different types of results (numerical and experimental),

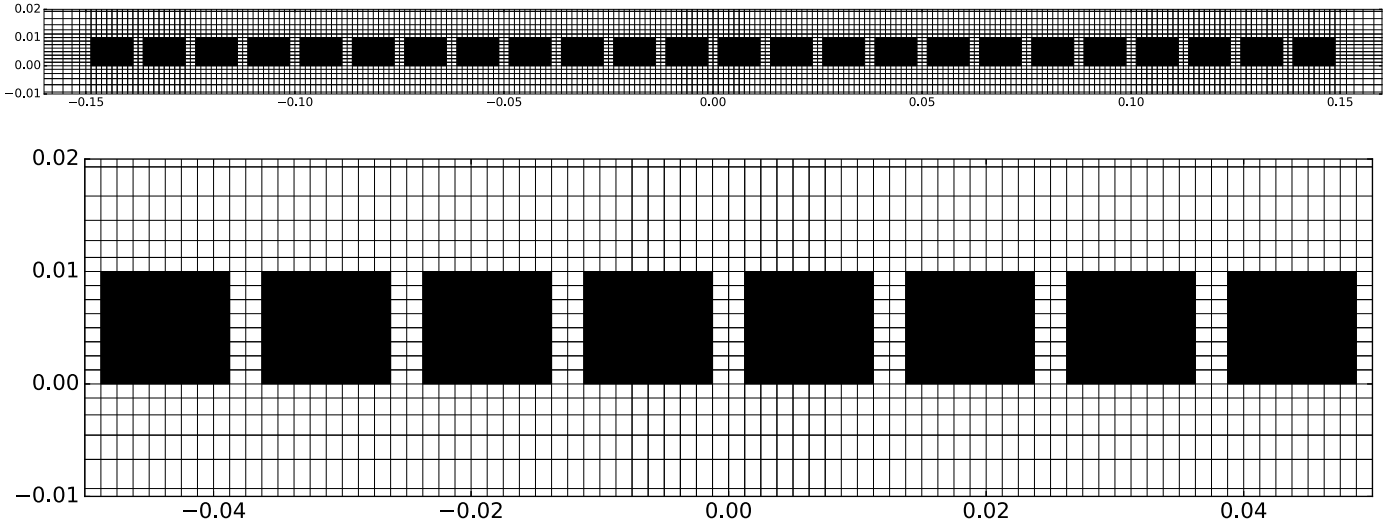

Fig. 14. Fine region grid of S19 (top). A zoomed-in section of the fine region grid is presented in the bottom subplot.

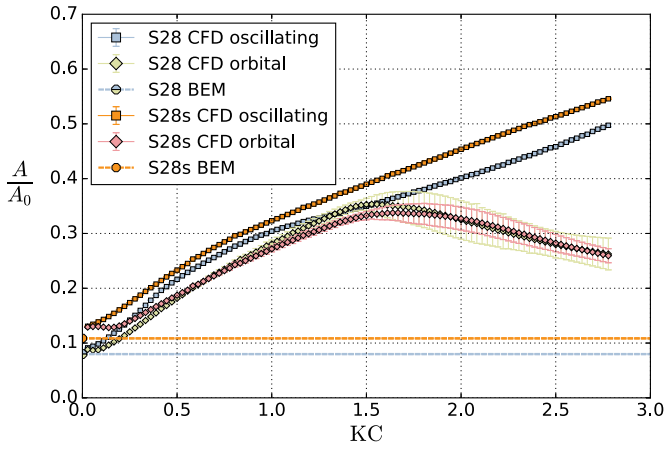

Fig. 16. Added mass coefficients from numerical simulations of oscillating flow conditions and orbital flow conditions for S28 and the simplified model, S28s.

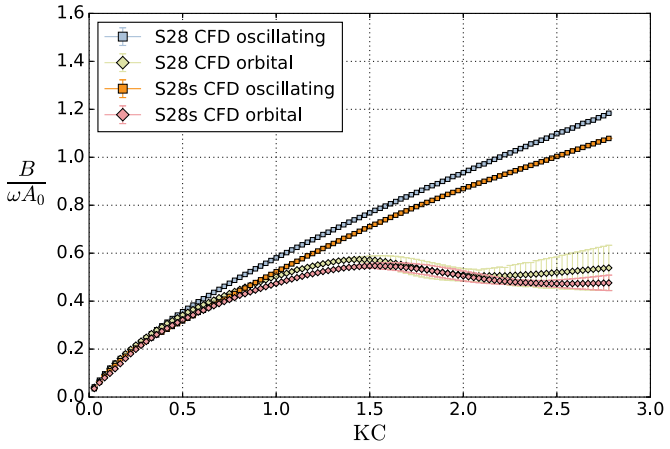

Fig. 17. Damping coefficients from numerical simulations of oscillating flow conditions and orbital flow conditions for S28 and the simplified model, S28s.

to investigate the effect of plate type and cylinder shape, is supported by the viscous flow solver results of S28, which are generally good compared to the experiments, cf. Fig. 13. However, we stress the added uncertainty of such an approach.

The results from the simulations of S19 are compared with the experimental results of C19 in Fig. 15. The added mass coefficient for S19 calculated with the potential flow solver is $\frac{A}{A_0} = 0.1438$. Both coefficients are larger for S19 than for C19 for corresponding KC numbers throughout the whole range of considered KC numbers. Based on the good agreement between the experimental and numerical results for S28, we are confident that the considerable differences between S19 and C19, by and large, must be a result of different cylinder shapes.

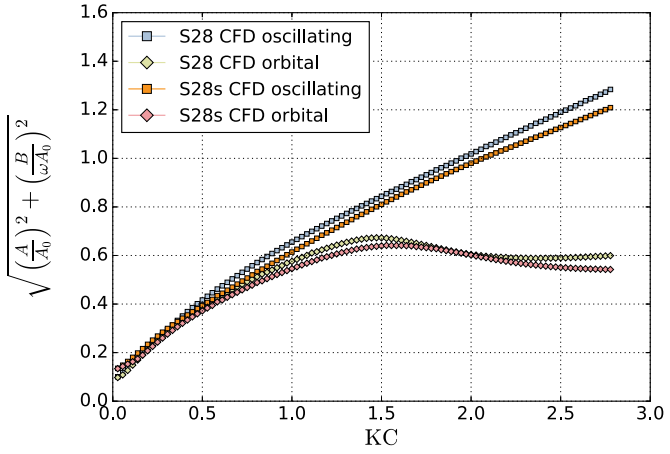

Fig. 18. Normalized force amplitude, i.e. the square root of the sum of the normalized added mass and damping coefficients squared, from numerical simulations of oscillating flow conditions and orbital flow conditions for S28 and the simplified model, S28s.

In the semi-analytical method by Molin for calculating the hydrodynamic coefficients of perforated plates, the effect of different types of openings of a perforated plate is expressed through the discharge coefficient, μ [6]. The discharge coefficient is inversely proportional to the resistance coefficient. In the case that the resistance is due to the drag of a cylinder, the discharge coefficient is inversely proportional to the drag coefficient. For a single cylinder of diameter $d = 0.01$ m, in the range of Reynolds number considered in the experimental investigations, cf. Section 3.4, the drag coefficient of a square cylinder is considerably larger than that of a circular cylinder, $\approx 50\% - 100\%$. Consequently, the drag coefficient for the row of square cylinders is likely considerably larger than that of the row of circular cylinders, although one must be careful with superposing the results due to the small distance between the cylinders, which gives speed-up of flow (increases the Reynolds number) and considerable interaction effects.

In Molin's original method without drag correction due to plate-end flow separation [6], the hydrodynamic coefficients only depend on the porous KC number, which can be written

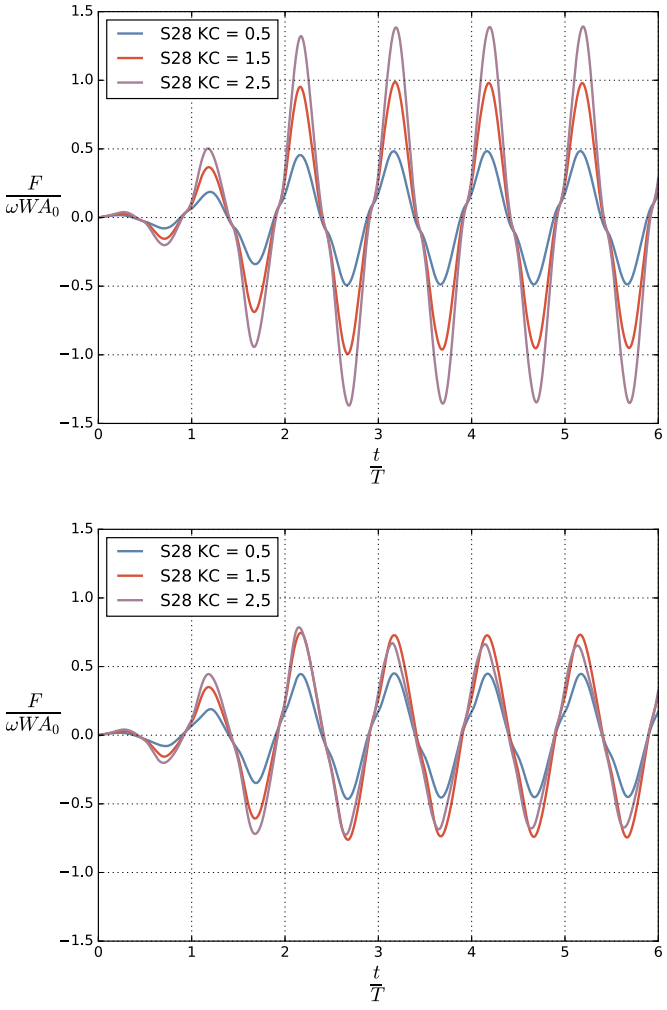

Fig. 19. Normalized force on S28 during the first six oscillation cycles for KC = 0.5, 1.5 and 2.5 from numerical simulations of oscillating (top) and orbital (bottom) flow conditions.

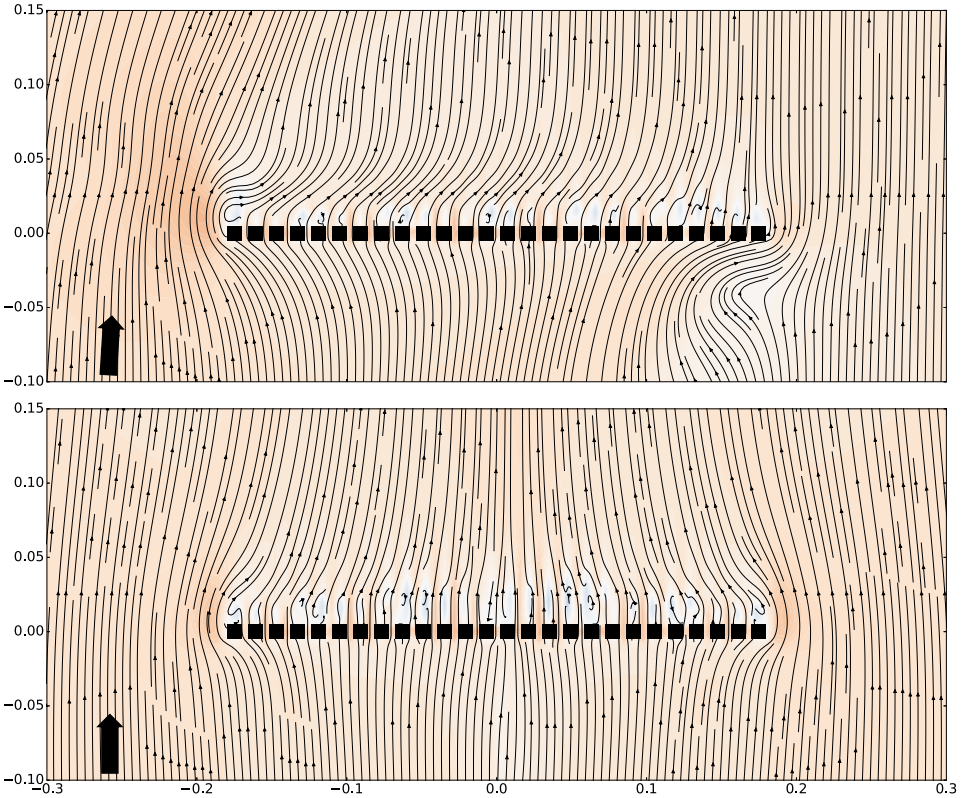

Fig. 20. Streamline plots of S28 with orbital (top) and oscillating (bottom) flow conditions at KC = 0.5. The time-instant is $0.26T$ into an oscillation period ($w = \frac{D}{T}\mathrm{KC}\sin\omega t$, orbital: $u = -\frac{D}{T}\mathrm{KC}\cos\omega t$, oscillating: $u = 0$). The color map for the contours represent the vertical velocity (red for positive, blue for negative). (For interpretation of the references to colour in this figure legend, the reader is referred to the web version of this article.)

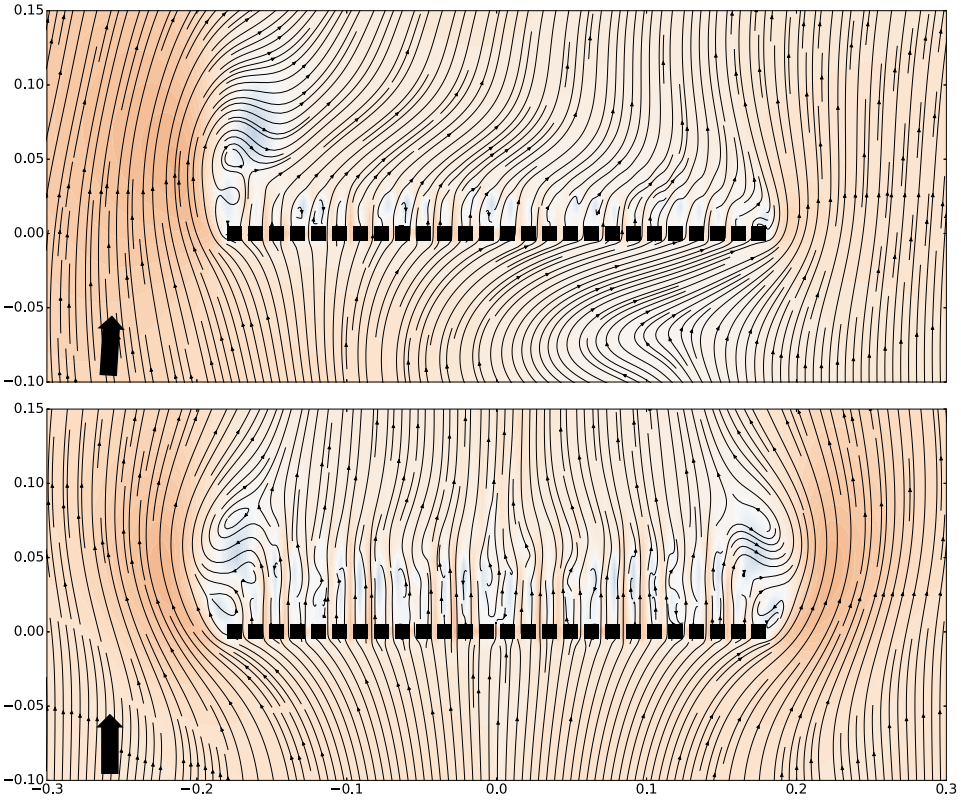

Fig. 21. Streamline plots of S28 with orbital (top) and oscillating (bottom) flow conditions at KC = 1.5. The time-instant is $0.26T$ into an oscillation period ($w = \frac{D}{T}\mathrm{KC}\sin\omega t$, orbital: $u = -\frac{D}{T}\mathrm{KC}\cos\omega t$, oscillating: $u = 0$). The color map for the contours represent the vertical velocity (red for positive, blue for negative). (For interpretation of the references to colour in this figure legend, the reader is referred to the web version of this article.)

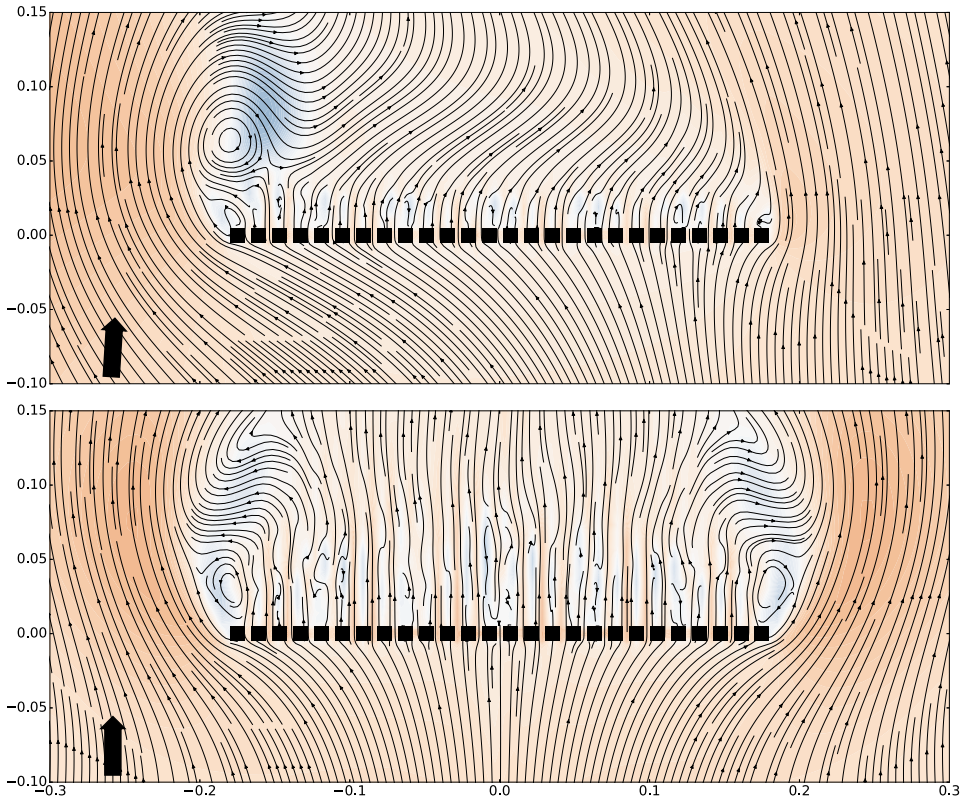

Fig. 22. Streamline plots of S28 with orbital (top) and oscillating (bottom) flow conditions at KC = 2.5. The time-instant is $0.26T$ into an oscillation period ($w = \frac{D}{T}\mathrm{KC}\sin\omega t$, orbital: $u = -\frac{D}{T}\mathrm{KC}\cos\omega t$, oscillating: $u = 0$). The color map for the contours represent the vertical velocity (red for positive, blue for negative). (For interpretation of the references to colour in this figure legend, the reader is referred to the web version of this article.)

$$\mathrm{KC}_{\mathrm{por}} = \mathrm{KC}\frac{1-\tau}{4\pi\mu\tau^2}, \tag{32}$$

hence increasing the drag coefficient (decreasing the discharge coefficient) is equivalent to increasing the KC number. The results of Fig. 15 supports the analysis of discharge coefficients since both coefficients increase with KC for both C19 and S19, and, for a given KC number, the coefficients are considerably larger for S19 than for C19. This is in particular true for the added mass of small KC numbers. However, the potential flow solver added mass calculated for S19 is almost twice that of C19, $\frac{A}{A_0} = 0.1438$ versus $\frac{A}{A_0} = 0.0780$. Therefore, it is likely that the large relative differences in added mass for small KC numbers is partly due to the difference in potential flow added mass of the two structures. Smaller relative differences for larger KC numbers can be an indication that the effect of plate-end flow separation is more important than the type of cylinder shape (and, for the added mass coefficients, potential flow effects) when the KC number is increased.

5.1.5. Orbital flow versus oscillating flow

Added mass and damping coefficients from the CFD simulations of orbital flow conditions are presented in Figs. 16 and 17. The normalized force amplitude, i.e. the square root of the sum of the normalized added mass and damping coefficients squared, Eq. (8), is presented in Fig. 18. The results are obtained for both S28 (26 squares) and the simpler model, S28s (11 rectangles), cf. Fig. 6. Oscillating flow results are included for comparison.

Consistent with the potential flow results, the S28s model yield slightly larger added mass coefficients than the S28 model in oscillating flow conditions. The damping coefficients show the opposite trend; the S28 model, which has smaller elements and more openings, yield larger damping coefficients than S28s. We do not observe the same clear tendencies in the orbital flow conditions, although the results at the smaller KC numbers corresponds to that of the oscillating flow conditions.

In general, the coefficients in orbital and oscillating flow are similar for small KC numbers, whereas there is a relative decrease in the orbital flow coefficients for increasing KC numbers. The presence of a non-zero horizontal velocity component in the orbital flow simulations is likely to affect the global flow separation, important for the force on the structure. We find it particularly interesting that there is a clear reduction in coefficients for $\mathrm{KC} \gtrsim 1.6$. Note that the KC number is defined based on the amplitude of the vertical velocity in both simulation types. Hence, the coefficients are smaller, even though the absolute velocities, $\sqrt{u^2 + w^2}$, are larger in orbital than in oscillating flow conditions for a given KC number.

In Fig. 19, the normalized vertical force time-series on the S28 plate is presented for three KC numbers, KC = 0.5, 1.5 and 2.5, for oscillating (top subplot) and orbital (bottom subplot) flow conditions. The normalized force is plotted against time for the first six periods of oscillation, including the ramp. In oscillating flow, Fig. 19, the normalized force increases with increasing KC. Contrary, the normalized force in orbital flow conditions reduces from KC = 1.5 to KC = 2.5, consistent with the results of Fig. 18.

Flow visualizations, comparing the orbital and oscillating flow fields, at KC = 0.5, 1.5 and 2.5, are analyzed. Streamline plots are presented in Figs. 20–22. The color map for the contours represent the vertical velocity (red for positive, blue for negative). The plots are zoomed in on the plates at a time-instant $0.26T$ into an oscillation period ($w = \frac{D}{T}\mathrm{KC}\sin\omega t$). Hence, at this time-instant, the boundary conditions are approximately equal in oscillating and orbital flow conditions; the vertical velocity is $w \approx W$, while the horizontal velocity is $u \approx 0$ (exactly $u = 0$ in oscillating flow conditions).

The flow visualizations at KC = 0.5 are presented in Fig. 20. The

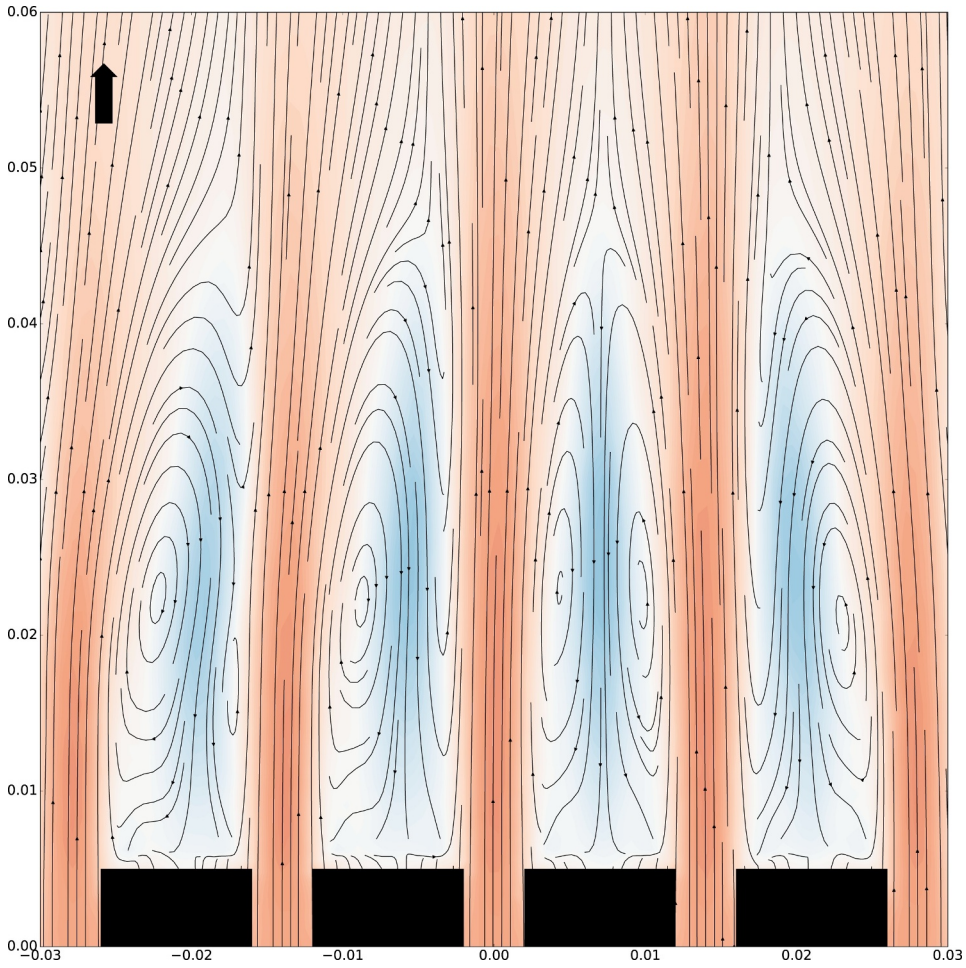

Fig. 23. Streamline plot zoomed in on the local flow separation from each of the four middle cylinders of S28 in oscillating flow at KC = 0.5. The time-instant is $0.26T$ into an oscillation period ($u = 0$, $w = \frac{D}{T}\mathrm{KC}\sin\omega t$). The color map for the contours represent the vertical velocity (red for positive, blue for negative). (For interpretation of the references to colour in this figure legend, the reader is referred to the web version of this article.)

normalized force amplitude is reduced by 7% in orbital compared to oscillating flow conditions at KC = 0.5. In both orbital and oscillating flow conditions, we observe local wakes downstream of each plate element of the perforated structure. The local wakes are of similar magnitude as the global vortical structures caused by flow separation at the plate-ends. A zoomed-in streamline plot illustrating the local flow separation from each cylinder of S28 is presented in Fig. 23. The streamlines are obtained for oscillating flow at KC = 0.5 at the time-instant $0.26T$.

Corresponding flow visualizations at KC = 1.5 are presented in Fig. 21. Here, the normalized force amplitude is 20% less in orbital than in oscillating flow conditions. The importance of the flow separation at the plate-ends, relative to the local flow separation at each plate element, is increased compared to KC = 0.5. In both flow conditions, there is a significant global wake formation downstream of the left plate-end, but only the oscillating flow has a similar wake downstream of the right plate-end. A reduction in flow velocity is observed upstream of the right plate-end in orbital flow.

As the KC number is further increased to KC = 2.5, Fig. 22, the extent of the global vortical structures from the plate-ends are considerably larger than the local vortical structures in the wakes behind each plate element. The reduction in the normalized force amplitude is 50% in orbital compared to oscillating flow conditions. A large plate-end vortex is observed on the left side only in orbital conditions, whereas a symmetric pattern is seen in oscillating flow. The fact that there is only one vortex rather than two, creating low pressure, might explain the lower force amplitude.

5.2. Damping-to-added mass ratio

The ratio of the damping force to the added mass force from the forced oscillation experimental investigations of C19 and S28, and the numerical simulations of S28 in oscillating and orbital flow conditions is presented in Fig. 24. Both configurations are damping dominant.

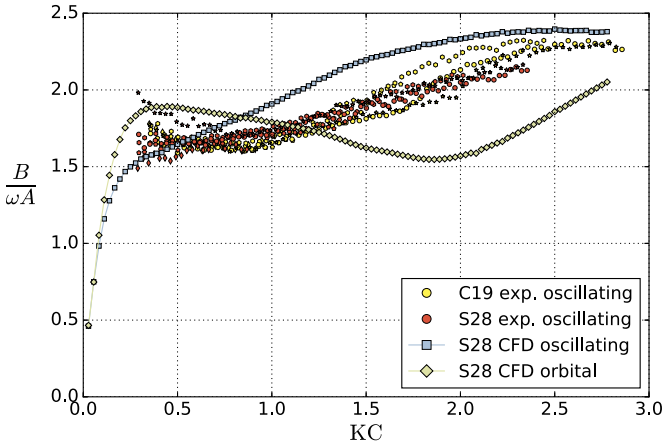

Fig. 24. Damping to added mass force ratio from forced oscillation experiments of C19 and S28 (five different periods of oscillation). Numerical results for S28 in forced oscillation and orbital flow conditions are included for comparison.

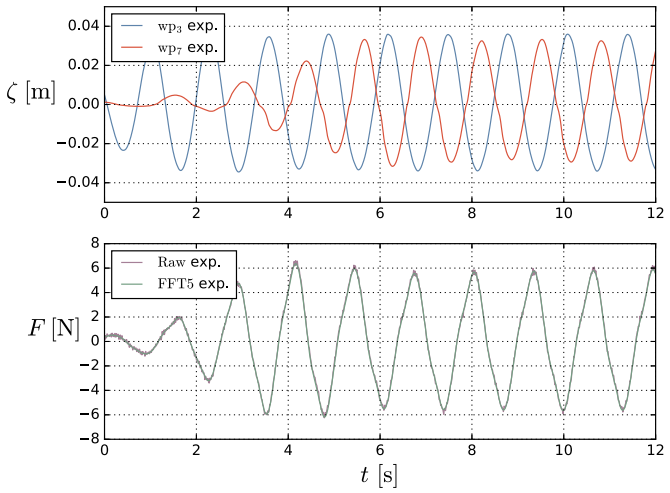

Fig. 25. Examples of time-series extracted from the experimental investigations of S28 in incident waves. The perforated plated is placed at $z_m = -0.3$ m. The wave parameters are $T = 1.3$ s and KC = 0.29. The wave elevations 2m upstream (wp_3) and 2m downstream (wp_7) of the model is presented, in addition to the raw and filtered force.

In a numerical study on the effect of perforation ratio, we found that the damping dominance increases, in general, with increasing perforation ratio [4]. This is consistent with previous experimental studies of perforated plates and disks [7,9,11]. However, despite the difference in perforation ratio for C19 ($\tau = 0.19$) and S28 ($\tau = 0.28$), there is no clear difference in their damping-to-added mass ratios. These findings suggest that the hydrodynamic force ratio is a function of both the perforation ratio and the shape of the perforated plate openings.

Although damping dominates in both orbital and oscillating flow, notable differences in the damping dominance are found between the two flow conditions. For small KC numbers, the damping dominance is larger in orbital than in oscillating flow conditions. For larger KC numbers, the opposite is observed.

5.3. Hydrodynamic force in incident waves

The hydrodynamic force on the perforated plates in incident waves is presented in the following. Examples of time-series extracted from the experiments are presented in Fig. 25. The measured wave elevations, 2m upstream and 2m downstream of the rig, and the force on the model are presented for the case of S28 placed at $z_m = -0.3$ m with wave parameters $T = 1.3$ s and KC = 0.29. In addition to the raw measurements, the force filtered around the first five harmonics is presented. We observe higher harmonics in the downstream wave measurements.

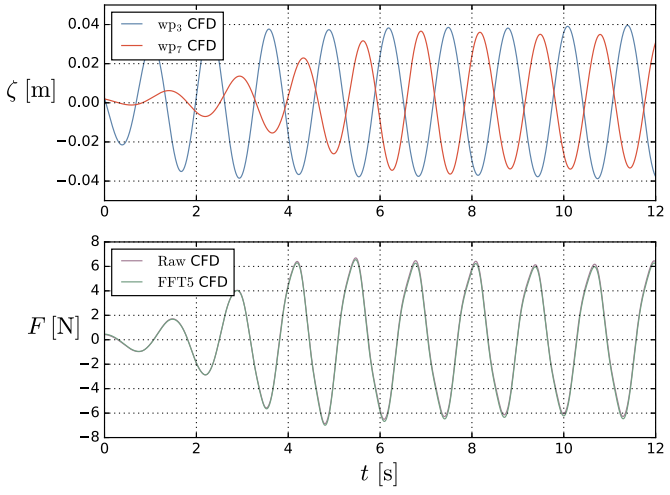

Fig. 26. Examples of time-series extracted from the numerical simulations of S28s in incident waves. The perforated plated is placed at $z_m = -0.3$ m. The wave parameters are $T = 1.3$ s and KC = 0.29. The wave elevations 2m upstream (wp_3) and 2m downstream (wp_7) of the model is presented, in addition to the raw and filtered force.

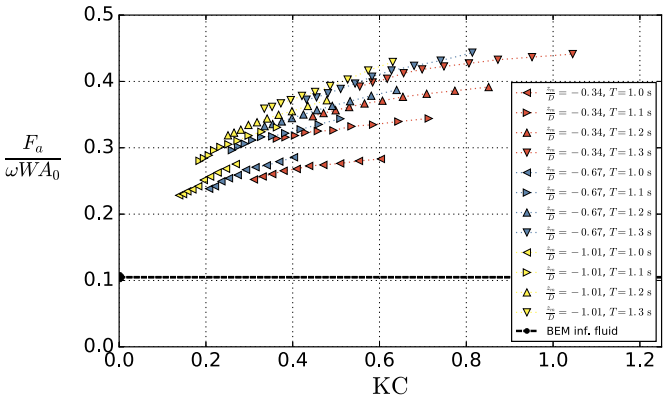

Fig. 27. Normalized force amplitude on C19. Results are presented for four wave periods, $T = 1.0$ s ($\frac{\lambda}{D} = 5.25$), $T = 1.1$ s ($\frac{\lambda}{D} = 6.35$), $T = 1.2$ s ($\frac{\lambda}{D} = 7.51$) and $T = 1.3$ s ($\frac{\lambda}{D} = 8.74$), with the model placed at $z = -0.30$ m, $z = -0.20$ m and $z = -0.10$ m.

In Fig. 26 we present the numerical counterpart of the experimental time-series of Fig. 25. Due to the hybrid numerical approach with linear free-surface conditions, the higher harmonics of the wave profiles in the experiments cannot be reproduced in the CFD. Contrary, the force on the plate, which is solved in the Navier–Stokes part of the domain, contains higher harmonics, similar to those in the experiments. Consequently, most of the nonlinearity in the force must be associated with the quadratic pressure jump on the plate. We note the good agreement between the numerical simulation and the experiment.

The normalized vertical force amplitude, from the experiments of C19 and S28 in waves, is presented in Fig. 27 for C19 and in Fig. 28 for S28. The experimental results are presented for three different submergences of the perforated plates, $z = -0.30$ m, $z = -0.20$ m and $z = -0.10$ m. Note that the Froude–Krylov force is not subtracted in these cases. Limiting values for KC $\to 0$ predicted by the potential flow solver in an infinite fluid domain are 0.1050 and 0.1054 for, respectively, C19 and S28, including the Froude–Krylov contributions, cf. Table 3. The potential flow calculations seem reasonable compared to the experimental results for both structures, contributing to confidence

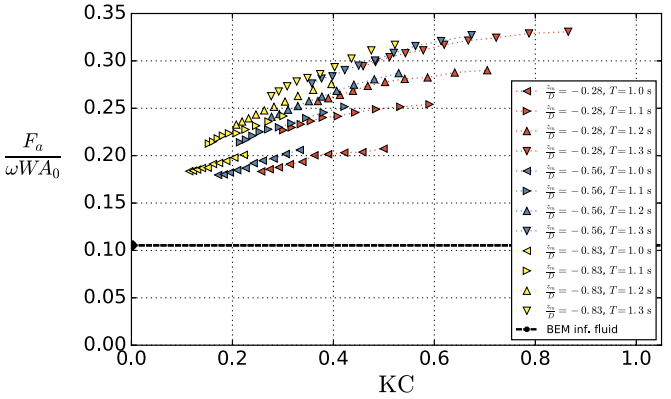

Fig. 28. Normalized force amplitude on S28. Results are presented for four wave periods, $T = 1.0$ s ($\frac{\lambda}{D} = 4.33$), $T = 1.1$ s ($\frac{\lambda}{D} = 5.23$), $T = 1.2$ s ($\frac{\lambda}{D} = 6.20$) and $T = 1.3$ s ($\frac{\lambda}{D} = 7.21$), with the model placed at $z = -0.30$ m, $z = -0.20$ m and $z = -0.10$ m.

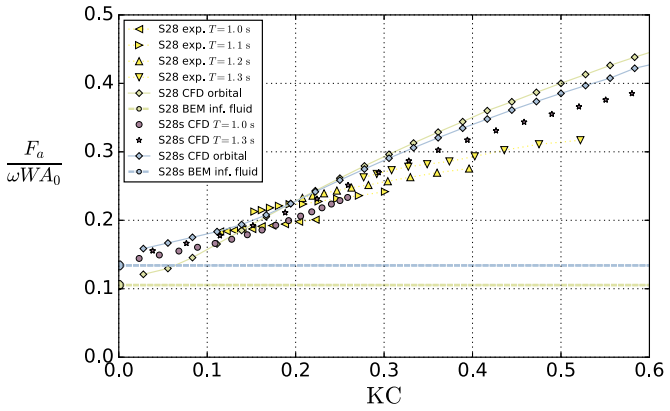

Fig. 29. Normalized vertical force amplitude on S28 and S28s, fixed in incident waves, from experiments and CFD. Experimental results for S28 are presented for four wave periods, $T = 1.0$ s ($\frac{\lambda}{D} = 4.33$), $T = 1.1$ s ($\frac{\lambda}{D} = 5.23$), $T = 1.2$ s ($\frac{\lambda}{D} = 6.20$) and $T = 1.3$ s ($\frac{\lambda}{D} = 7.21$), with the model placed at $z = -0.30$ m. CFD results for S28s are presented for two wave periods, $T = 1.0$ s ($\frac{\lambda}{D} = 4.33$) and $T = 1.3$ s ($\frac{\lambda}{D} = 7.21$), with the model placed at $z = -0.30$ m. Orbital flow simulations and BEM results for S28 and S28s are included for comparison.

in the experiments.

The normalized force on C19 is, in general, larger than the force on S28 for a given KC number. The overall trends are similar for the normalized force on the two models. The force increases, in general, with increasing KC number also in waves.

The normalized force in waves depends on both the wave period and the submergence. Some period dependence is noted, in particular for larger KC numbers and for increasing wave steepnesses. For a given KC number, increasing the wave period—which increases $\frac{\lambda}{D}$ and $\frac{\lambda}{2\zeta_a}$—increases, in general, the normalized force amplitude. The variations in the flow over the plates are larger when $\frac{\lambda}{D}$ is small, which is a likely explanation. The sensitivity to the vertical position is, in general, small when the depth dependence of the velocity is included in the normalization of the force amplitude. This is in particular true for the longest waves. However, there is a tendency that the normalized force is slightly increased when the distance from the free-surface is increased, given a fixed KC number.

In Fig. 29, CFD results of S28 and S28s are presented. The CFD includes numerical simulations of S28s at $z = -0.30$ m including linearized free-surface conditions, as well as orbital flow simulations of S28 and S28s. The KC numbers of the linearized free-surface CFD are based on the calculated wave elevations above the center of the model, cf. ζ_a in Eq. (2). The experimental results with the model placed at $z = -0.30$ m are included for comparison. There is in general good agreement between the numerical simulations of incident waves and the experiments.

The orbital flow simulations of S28 were included in Fig. 29 as well. For KC $\gtrsim 0.3$, the force is overpredicted in orbital flow relative to the experiments and CFD with waves. However, for KC $\lesssim 0.3$, the force is very similar to that in waves. This is interesting from a practical point of view, since the orbital flow simulations are significantly less cumbersome. In terms of safety, the most conservative approach (oscillating, orbital or waves) to choose in a practical situation, is likely to be coefficients based on oscillating flow.

In Figs. 30 and 31, streamline plots for S28s are presented. The incident wave simulation with wave parameters $T = 1.3$ s, $\frac{\lambda}{D} = 7.21$ and KC $= 0.52$ is compared with the orbital flow simulation of KC $= 0.50$. The normalized force amplitude on the models is similar for these cases, cf. Fig. 29.

The streamline plots are matched with regards to the vertical velocity at the free surface above the centerline of the plate in the incident wave simulation. In Fig. 30, the vertical velocity at the free-surface above the center of the plate is at its maximum. In the orbital simulation, the horizontal velocity is zero, whereas in the incident wave

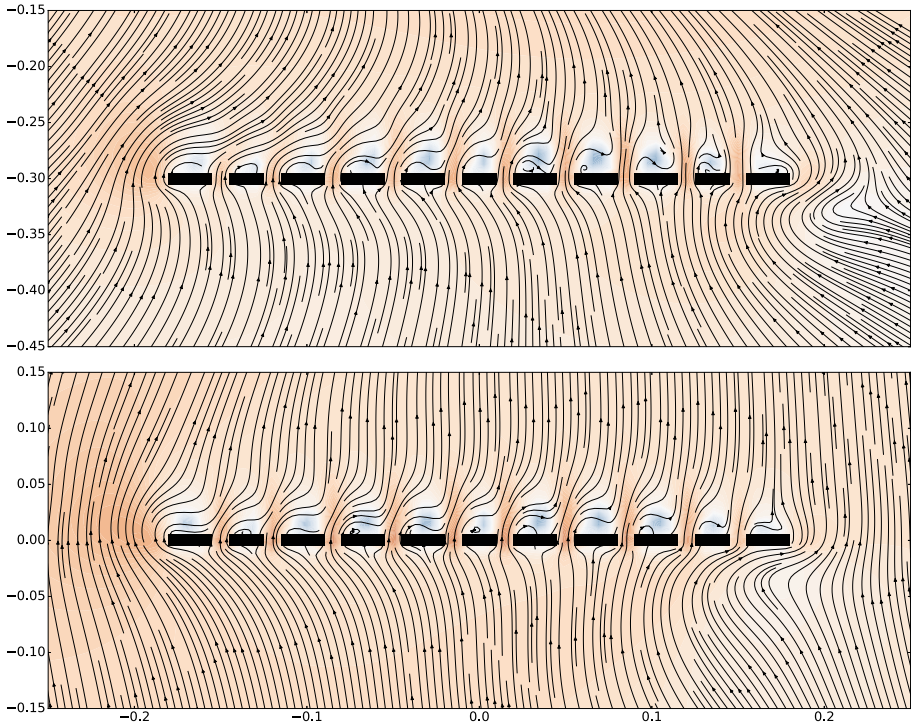

Fig. 30. Streamline plots for KC $= 0.5$ from the numerical incident wave (top) and orbital (bottom) simulations of S28s. In the incident wave simulation, the time-instant is taken when the vertical velocity above the centerline of the plate is at its maximum. In the orbital simulation, the time-instant is $0.24T$ into an oscillation period ($u = -\frac{D}{T}\text{KC}\cos\omega t$, $w = \frac{D}{T}\text{KC}\sin\omega t$). The color map for the contours represent the vertical velocity (red for positive, blue for negative). (For interpretation of the references to colour in this figure legend, the reader is referred to the web version of this article.)

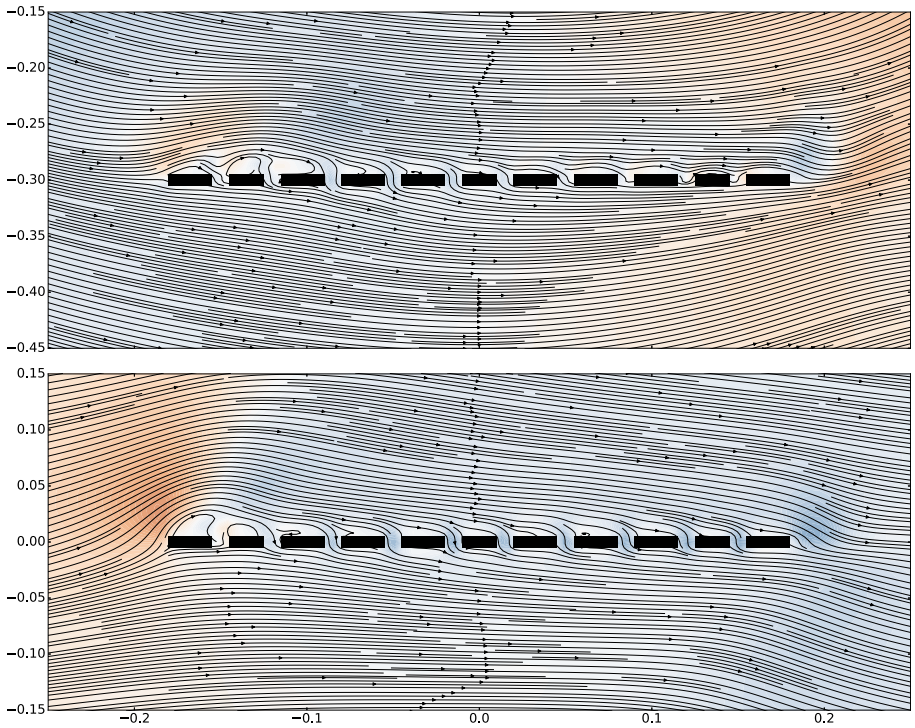

Fig. 31. Streamline plots for KC = 0.5 from the numerical incident wave (top) and orbital (bottom) simulations of S28s. In the incident wave simulation, the time-instant is taken when the vertical velocity above the centerline of the plate is zero. In the orbital simulation, the time-instant is $0.50T$ into an oscillation period ($u = -\frac{D}{T}\mathrm{KC}\cos\omega t$, $w = \frac{D}{T}\mathrm{KC}\sin\omega t$). The color map for the contours represent the vertical velocity (red for positive, blue for negative). (For interpretation of the references to colour in this figure legend, the reader is referred to the web version of this article.)

simulation the horizontal velocity is positive upstream and negative downstream of the centerline of the plate. In Fig. 31, the vertical velocity at the free-surface above the center of the plate is zero (positive upstream and negative downstream), and the horizontal velocity is positive. Contrary, in the orbital flow simulation, the ambient vertical velocity is zero in the whole domain.

6. Conclusion

The hydrodynamic forces and behavior of two-dimensional perforated plates, relevant for several marine applications, were investigated. Experiments and simulations were performed in forced oscillations, waves and orbital flow. Good agreement between experimental and numerical results were found. Therefore, streamline plots were used to study the flow in detail.

Added mass and damping coefficients were presented for oscillating and orbital flow conditions. Consistent with previous investigations, the hydrodynamic force on the structures, which have perforation ratios $\tau = 0.19$ and $\tau = 0.28$, are dominated by damping. Further, we find that the forces and coefficients of the perforated structures are functions of the amplitude of motion. The period dependence is small in oscillating flow.

Considerable differences are found in the hydrodynamic forces in oscillating and orbital flow conditions. An exception is for small $\mathrm{KC} \lesssim 0.5$. In both conditions, streamline plots reveal that the relative importance of vortex generation from the plate-ends, compared to the local flow separation from each plate element, increases with increasing KC number. Decreased force in orbital compared to oscillating flow was found for all simulated configurations, with increasing relative importance for increasing KC number. We emphasized the influence from plate-end flow separation, which is asymmetric in orbital flow.

The normalized force amplitude on the perforated plates in waves increases, in general, with increasing KC number. The period dependence increases with decreasing distance to the mean free surface. For small and moderate KC numbers, orbital flow simulations give a good prediction of the force in waves. For larger KC numbers, orbital flow simulations overpredict the force.

Author statement

This research was carried out in collaboration between both authors.

Fredrik Mentzoni: Carried out the experiments, planned the model tests, carried out the numerical simulations and wrote the manuscript.

Trygve Kristiansen: Participated in planning of model tests and took part in writing the manuscript.

Both authors read and approved the final manuscript.

Declaration of Competing Interest

The authors declare that they have no known competing financial interests or personal relationships that could have appeared to influence the work reported in this paper.

Acknowledgement

This work was financed by the Research Council of Norway, NFR project 237929 CRI MOVE.

Appendix A. Experimental time-series

Figs. A.32 –A.39.

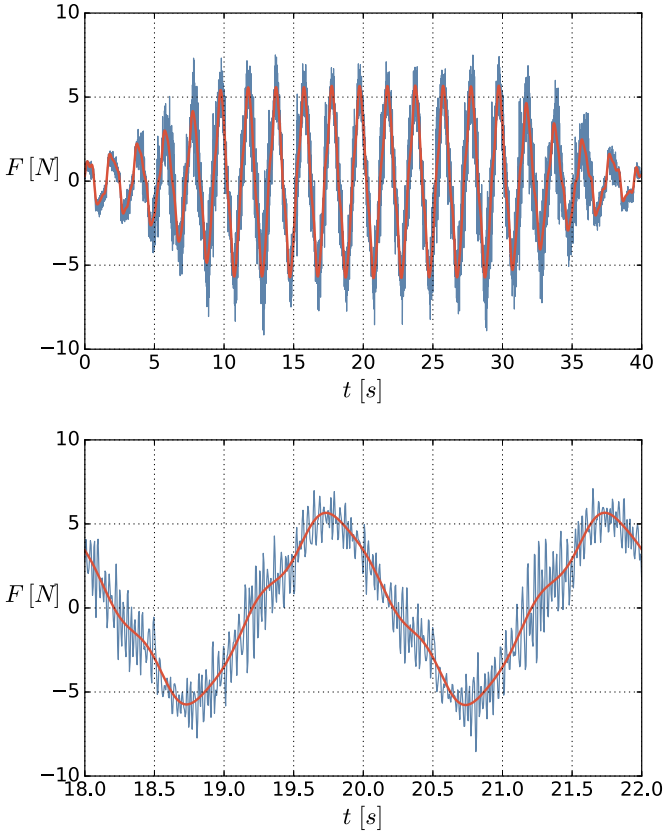

Fig. A.32. Forced oscillation experiments of C19. T = 2.0 s, η_a= 1.7 cm, KC = 0.35. Measured and filtered force.

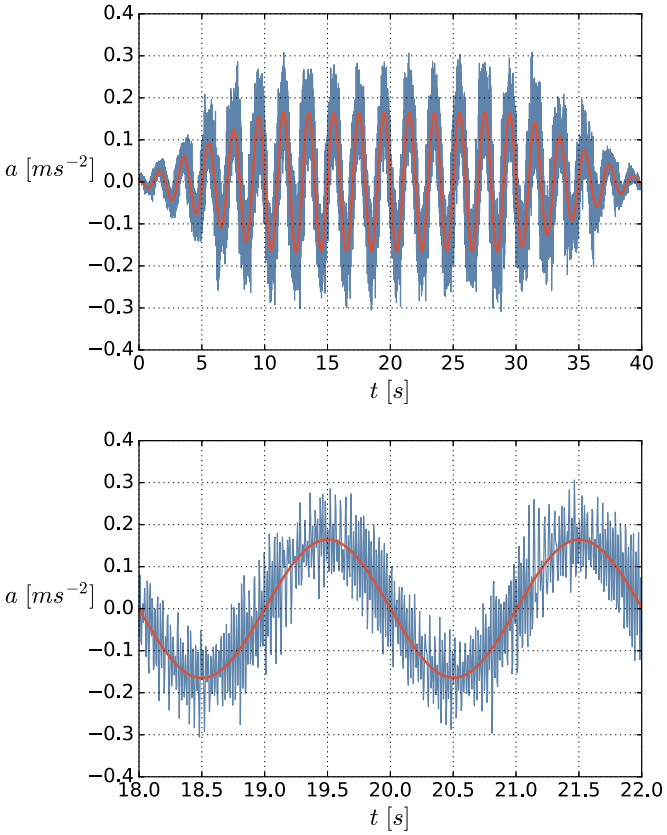

Fig. A.33. Forced oscillation experiments of C19. T = 2.0 s, η_a= 1.7 cm, KC = 0.35. Measured and filtered acceleration.

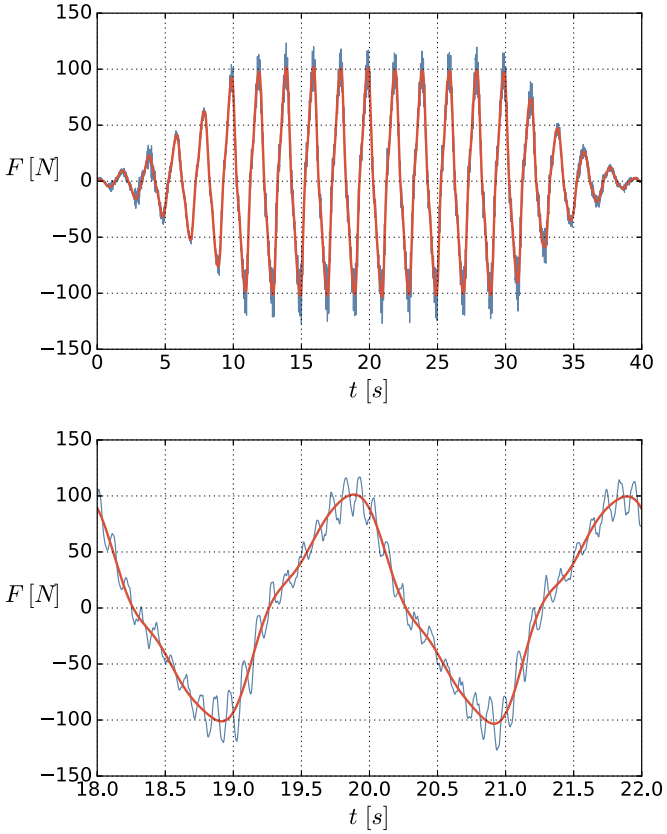

Fig. A.34. Forced oscillation experiments of C19. T = 2.0 s, η_a=13 cm, KC = 2.82. Measured and filtered force.

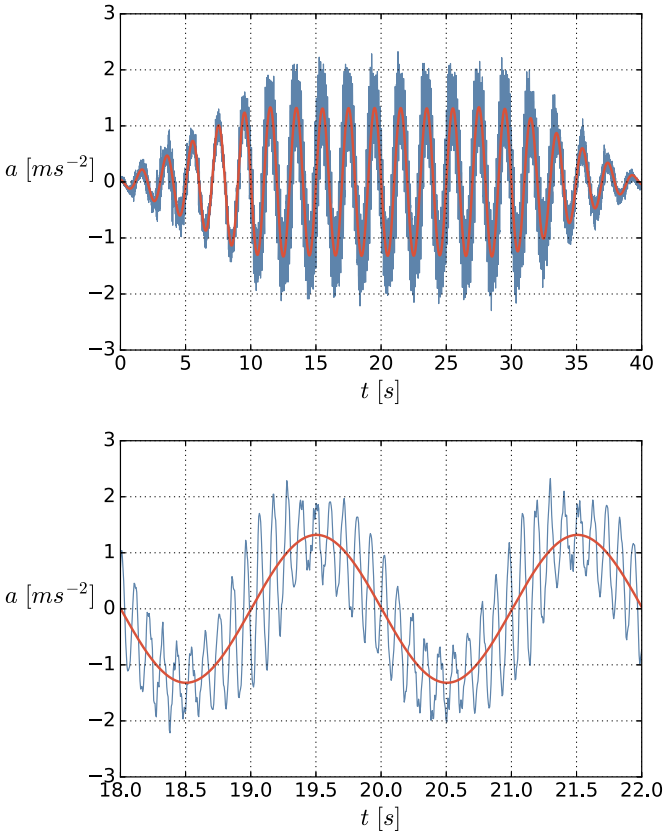

Fig. A.35. Forced oscillation experiments of C19. T = 2.0 s, η_a = 13 cm, KC = 2.82. Measured and filtered acceleration.

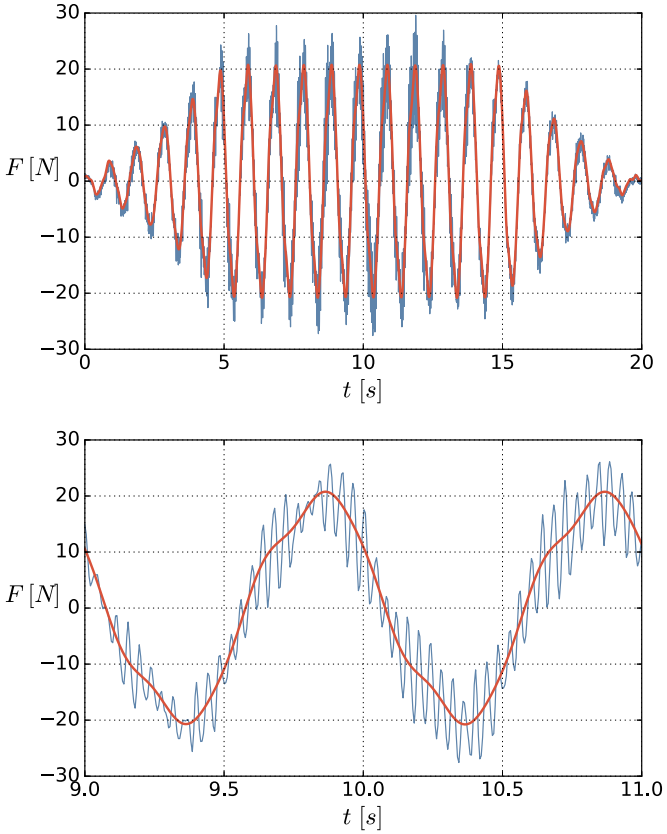

Fig. A.36. Forced oscillation experiments of C19. $T = 1.0$ s, $\eta_a = 1.7$ cm, KC = 0.35. Measured and filtered force.

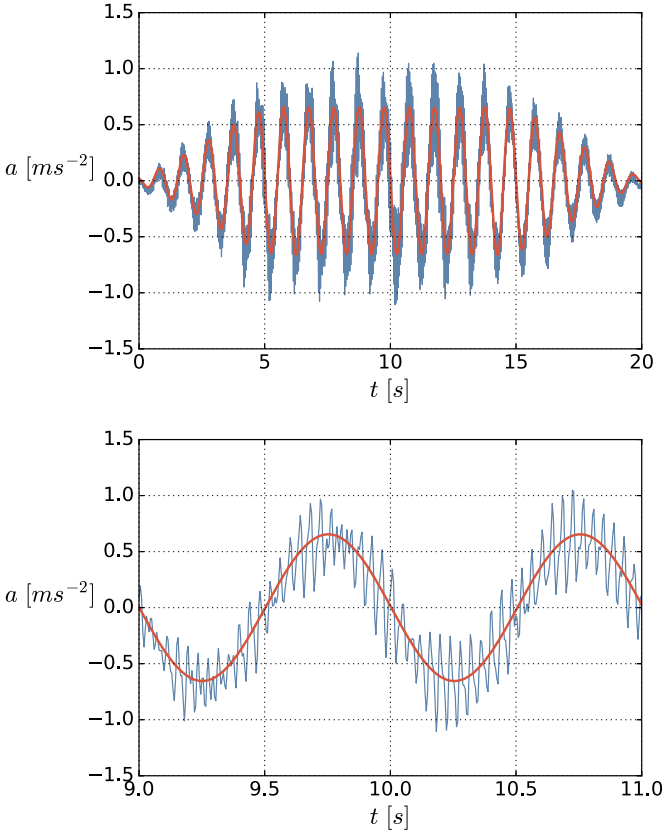

Fig. A.37. Forced oscillation experiments of C19. $T = 1.0$ s, $\eta_a = 1.7$ cm, KC = 0.35. Measured and filtered acceleration.

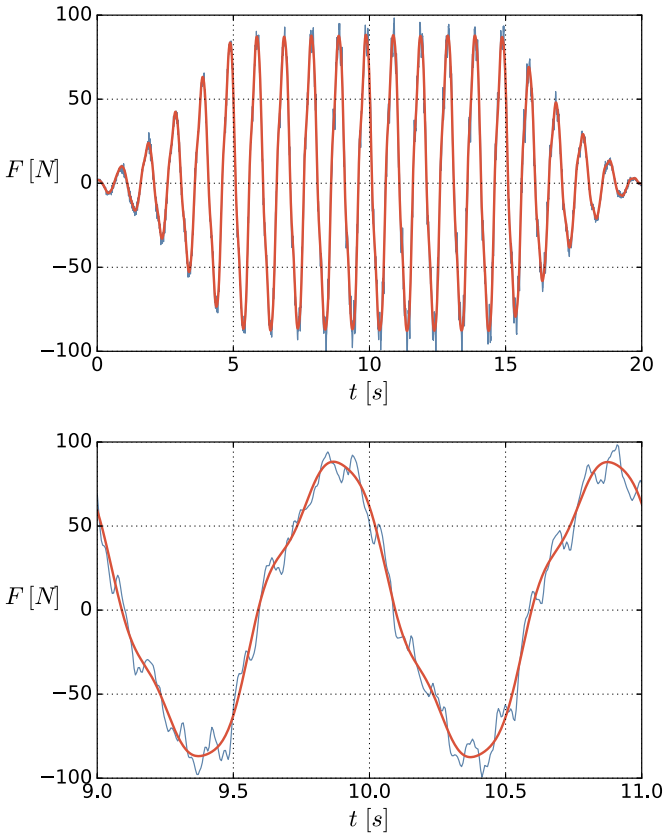

Fig. A.38. Forced oscillation experiments of C19. $T = 1.0$ s, $\eta_a = 5.0$ cm, KC = 1.05. Measured and filtered force.

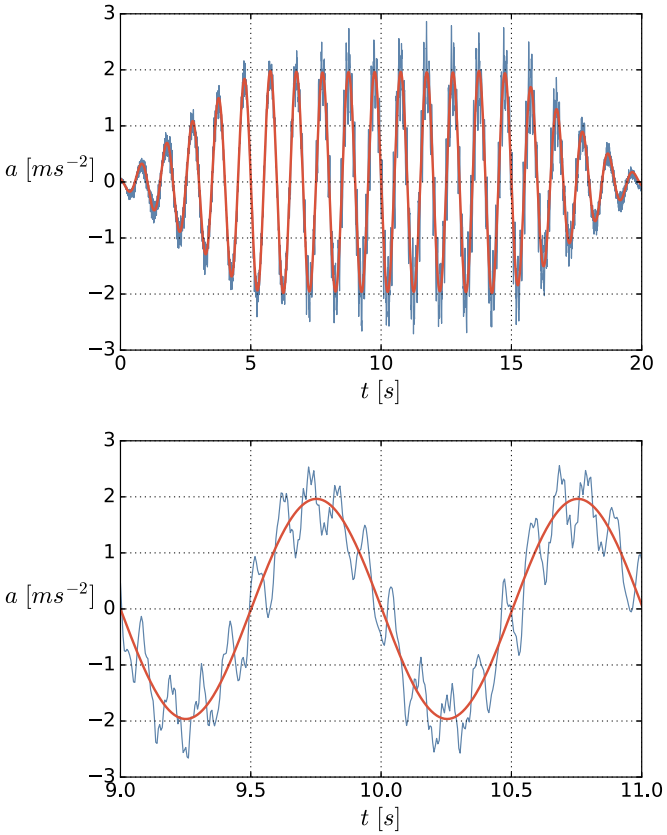

Fig. A.39. Forced oscillation experiments of C19. $T = 1.0$ s, $\eta_a = 5.0$ cm, KC = 1.05. Measured and filtered acceleration.

References

[1] F. Mentzoni, T. Kristiansen, Two-dimensional experimental and numerical investigations of parallel perforated plates in oscillating and orbital flows, Appl. Ocean Res. 97 (2020) 102042.

[2] F. Mentzoni, M. Abrahamsen-Prsic, T. Kristiansen, Hydrodynamic coefficients of simplified subsea structures, omae2018-78315, Proceedings of the International Conference on Offshore Mechanics and Arctic Engineering, (2018).

[3] F. Mentzoni, T. Kristiansen, Numerical modeling of perforated plates in oscillating flow, Appl. Ocean Res. 84 (2019) 1–11.

[4] F. Mentzoni, T. Kristiansen, A semi-analytical method for calculating the hydrodynamic force on perforated plates in oscillating flow, omae2019-95093, Proceedings of the International Conference on Offshore Mechanics and Arctic Engineering, (2019).

[5] F. Solaas, F. Mentzoni, M. Abrahamsen-Prsic, T. Kristiansen, An experimental and numerical study of added mass and damping for side by side plates in oscillating flow, omae2019-96008, Proceedings of the International Conference on Offshore Mechanics and Arctic Engineering, (2019).

[6] B. Molin, Hydrodynamic modeling of perforated structures, Appl. Ocean Res. 33 (1) (2011) 1–11.

[7] P.C. Sandvik, F. Solaas, F.G. Nielsen, Hydrodynamic forces on ventilated structures, Proceedings of the International Offshore and Polar Engineering Conference, (2006), pp. 54–58.

[8] L. Tao, D. Dray, Hydrodynamic performance of solid and porous heave plates, Ocean Eng. 35 (10) (2008) 1006–1014.

[9] S. An, O.M. Faltinsen, An experimental and numerical study of heave added mass and damping of horizontally submerged and perforated rectangular plates, J. Fluids Struct. 39 (2013) 87–101.

[10] J. Li, S. Liu, M. Zhao, B. Teng, Experimental investigation of the hydrodynamic characteristics of heave plates using forced oscillation, Ocean Eng. 66 (2013) 82–91.

[11] X. Tian, L. Tao, X. Li, J. Yang, Hydrodynamic coefficients of oscillating flat plates at 0.15 KC 3.15, J. Mar. Sci. Technol. 22 (1) (2017) 101–113.

[12] B. Molin, On the added mass and damping of periodic arrays of fully or partially porous disks, J. Fluids Struct. 15 (2) (2001) 275–290.

[13] O.M. Faltinsen, Sea Loads on Ships and Offshore Structures, Cambridge Ocean Technology Series, Cambridge University Press, 1993.

[14] A.J. Chorin, Numerical solution of the Navier-Stokes equations, Math. Comput. 22 (104) (1968) 745–762.

[15] T. Kristiansen, O.M. Faltinsen, Gap resonance analyzed by a new domain-decomposition method combining potential and viscous flow draft, Appl. Ocean Res. 34 (2012) 198–208.

[16] J.N. Newman, Marine Hydrodynamics, The MIT Press, MIT Press, 1977.